Use Authorization

Use Authorization In presenting this dissertation in partial fulfillment of the requirements for an advanced degree at Idaho State University, I agree that the Library shall make it freely available for inspection. I further state that permission to download and/or print my dissertation for scholarly purposes may be granted by the Dean of the Graduate School, Dean of my academic division, or by the University Librarian. It is understood that any copying or publication of this dissertation for financial gain shall not be allowed without my written permission.

Signature _____

Date _____

The Performance of a Fission Chamber equipped with Gaseous Electron Multiplier (GEM) Preamplifiers

by

Haitham Abdel Majid

A dissertation

submitted in partial fulfillment

of the requirements for the degree of

Doctor of Philosophy in the Department of Physics

Idaho State University

November 2015

To the Graduate Faculty:

The members of the committee appointed to examine the dissertation of Haitham Abdel Majid find it satisfactory and recommend that it be accepted.

Tony Forest, Ph.D.

George Imel, Ph.D

Khalid Chouffani, Ph.D.

Eddie Tatar, Ph.D

Tony Hill, Ph.D.

I dedicate this work for my family, specially for my mother Sharifah who was supportive and patiently waited for this moment, but she peacefully left this world before I reached home. Additionally, I dedicate this work for my five year old daughter Serene who always lives in my heart even if she is physically far away. I dedicate it for my friends and all the people who supported me from inside and outside the United States.

TABLE OF CONTENTS

LIST OF FIGURES

LIST OF TABLES

Abstract

A new type of fission chamber was designed, constructed, and tested using α-particles emitted by a thin U-233 source that is capable of operating, in pulse mode, at detection rates of 0.5 MHz and provide position information to less than a millimeter. The typical fission chamber is in the form of a cylinder with a coating of fissionable material on its inside surface and an electrode at its center for collecting electrons liberated by fission fragments that are amplified as they are attracted to the central wire due to an electric field created when the wire is held at a fixed voltage. The fission chamber in this work replaces the cylinder and wire with a planar geometry that uses a new method to amplify the electrons ionized by a fission fragment and collect those ions on a grid that provides spatial information. The result is a fission chamber with the potential to improve many applications that involve neutron imaging, non-destructive testing (NDT), and others that wish to determine the location of a neutron in an environment with high neutron fluence.

Chapter 1

Physical Concepts and Theories

Radioisotopes, such as U-233, emit α, β and γ particles which interact with the surrounding medium. If the medium is gasoues, the emitted particles from a U-233 coating lose their energy by colliding with the atoms and molecules of the medium, which mostly leads to the ionization of the gas. Depending on the deposited energy in the medium, primary electrons are liberated with kinetic energies that could ionize the gas again liberating secondary electrons. If an electric field is present in the gas, it will transport and accelerate the free electrons to prevent them from being captured until the free electrons collide with the low voltage electrode. This chapter describes the interactions of α, β and γ-particles with a gaseous medium to predict the detector's performance.

1.1 Radioactive Decay

1.1.1 α-Particle Emission

Rutherford and Chadwick[1] studied α-emission from a classical point of view. Classically, it should have been impossible to emit α-particles from the nucleus. However, they were experimentally observed when Rutherford and Chadwick exposed U-nuclei to 9 MeV α-particles. Unfortunately, they did not observe any α-particle scattering from the target nuclei as they observed in the α-particles scattering from the gold foil experiment. Thus, Rutherford and Chadwick could not illustrate α-emission from a classical point of view since they thought that the α-particle was surrounded by a minimum of a 9 MeV potential barrier.[1]

However, α-emission was thoroughly studied after the development of quantum mechanics, specifically after the tunneling effect (or quantum tunneling phenomenon). The core of quantum mechanics is based on probability, which gives scientists the flexibility to study any system if the wave function is known. The tunneling effect involves the possibility that an α-particle will escape from the nucleus after frequently encountering its barrier.

The technique starts with determining the Coulomb potential for the system's Hamiltonian, which is represented by Equation 1.1.

$$V = 2Ze^2/r \tag{1.1}$$

Equation 1.2 shows the scattering S-wave solution for an α-emission by the WKB method[1]

$$\psi(r) = exp\left[\frac{2}{\hbar}\int_R^{2Ze^2/E}\sqrt{2\mu\left(\frac{2Ze^2}{r} - E\right)}\mathbf{dr}\right] \tag{1.2}$$

where Z is the atomic number of the daughter nucleus, R is the radius of the daughter nucleus, μ is the reduced mass of the α-particle and mass of the daughter nucleus, and E is the corrected α-particle recoil energy. Considering the screening effect as reviewed by Perlman and Rasmussen in Equation 1.3 in eV units,[1]

$$\Delta E_{sc} = 65.3\,(Z+2)^{7/2} - 80\,(Z+2)^{2/5} \tag{1.3}$$

would redefine the decay energy to E + ΔE_{sc}, so Equation 1.2 is written as shown in Equation 1.4, where B is the potential barrier height.[1]

$$\psi(r) = \exp\left[\frac{-2}{\hbar}\,(2MB)^{1/2}\,R\left(X^{-1/2}cos^{-1}X^{1/2} - (1-X)^{-1/2}\right)\right] \tag{1.4}$$

$$X = \frac{E_{eff}}{2Ze^2} = \frac{E_{eff}}{B}$$

$$B = \frac{2Ze^2}{R}$$

Finally, Equation 1.5 shows how to calculate the decay constant using ψ(r), here f is the number of collisions per second.[1]

$$\lambda = f\psi(r) \tag{1.5}$$

In spite of the dominant transitions to the nuclear ground state in U-233 and Th-232, the α-transition are restricted by a selection rule. α-particles have a zero spin and an even parity, so the initial and final state is dependent on the angular momentum as is shown in Equation 1.6. Therefore, L can be an even or an odd value if the parities are similar. If the parities are opposite, the special rule for even-even nuclei says, "all of the even-spin states have even parity and all the odd-spin states have odd-parity."[1]

$$|l_i - l_f| \leq L \leq |l_i + l_f| \tag{1.6}$$

where L is the orbital angular momentum, and l_i and l_f are the angular momentum eigenvalues for the transition's initial and final state. Figure 1.1 shows the α-decay schemes for U-233 and Th-232.

α-decay in odd-A nuclei is different from that of the even-even nuclei due to the rotational characteristics of the ground state (degeneracy) for each type of nuclei. Th-232 and U-233 represent two different types of nuclei that emit α-particles through the transition to the ground state. For Th-232, the ground state has L=0, which makes it the most likely transition as shown in Figure 1.1-b. On the other hand, the ground state of U-233 has L=+5/2, which generates a rotational band for the ground state that competes with the main transition to the ground state as shown in Figure 1.1-a. As a result, the range of energy of the emitted α-particles from U-233 has an energy range of 4.5-4.85 MeV with 12 transitions, compared to that of Th-232, which only has 3 transitions at an energy range of 3.82-4.00 MeV.[1]

The ratio of the reduced α-decay widths (Hindrent factors)for the ground state-to-ground state decay to the decay width to the excited state in the daughter nucleus

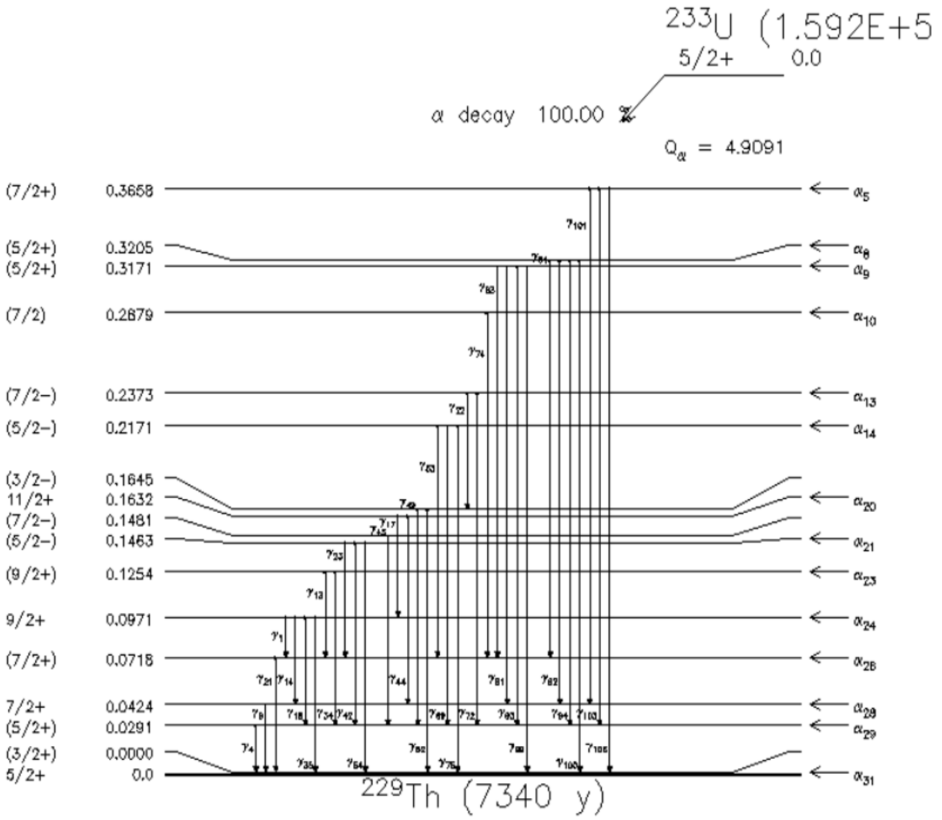

(a)

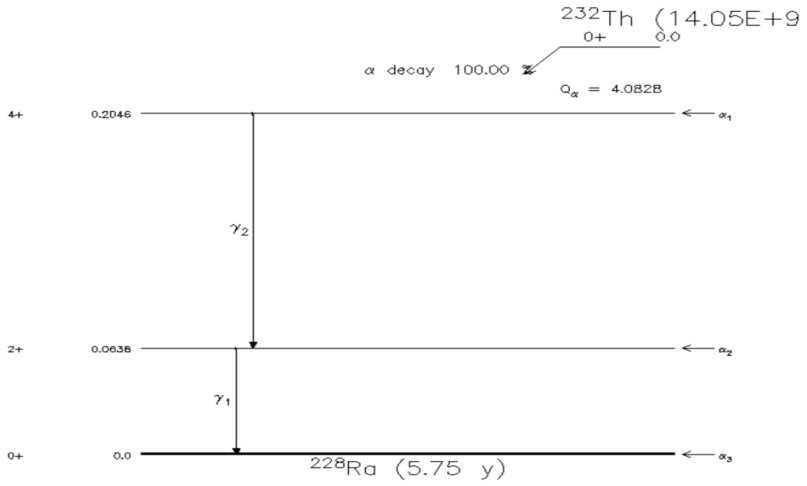

(b)

Figure 1.1: Energy level scheme for U-233 and Th-232 α-decay.[2]

Alpha emitter	Energy of final state (keV)	Hindrent factor	Emission Percentage (%)
Th-232	59 (+2)	0.545	21.7
U-233	0	1.17	84.3
	42.8	3.7	13.6
	98.9	10.5	1.61
	166	180	0.042
	316	13	0.012
	365	60	0.0028

Table 1.1: Final states energy with hindrent factors along with emission percentages for Th-232 and U-233.[1][2]

determines the probability of α-emission.[3] It gives unity for the ground state of even-even nuclei and close to a unity for odd-A nuclei.[1] Table 1.1 shows the nuclear energy states with difference in energy for successive states and the hindrance factor for each nuclear state of U-233 and Th-232[1] and their emission percentages.[2]

1.1.2 β^-Particles Emission

β^--particle emission occurs when an unstable nucleus undergoes neutron decay to a proton and an electron and then ejects the electron out of the nucleus. Equation 1.7 shows the neutron decay products which have the antineutrino $\bar{\nu}$ as a neutral particle to conserve of linear momentum for the products. The electron leaves the nucleus as a β^--particle along with the antineutrino sharing the decay energy of the interaction.

$$n \rightarrow p + \beta^- + \bar{\nu} \tag{1.7}$$

The β^--particle separate energy is the difference in mass of the mother and the daughter nuclei after subtracting the$\bar{\nu}$ kinetic energy. The sum of the kinetic energy of a β^--particle and the kinetic energy of an $\bar{\nu}$ is directly proportional to the difference in mass of the mother and the daughter nuclei, and the β^--particle energy is what remained after subtracting the $\bar{\nu}$ energy. However, if the daughter nucleus is a γ-emitter, the kinetic energy of the emitted β^--particle will drop equivalent to the energy of the emitted γ-rays, and total decay energy Q_β is defined as shown in Equation (1.8).[4]

$$Q_{\beta^-} = K.E_T = E_{\beta^-} + E_\gamma + E_{\bar{\nu}} + E_{recoil} \tag{1.8}$$

As a rule of thumb, the emitted β^--particles have a wide continuous spectrum, and the majority of them have an energy of $(1/3)E_{max}$. The main reason for the wide energy range for β^--decay is due to the sharing of kinetic energy with the $\bar{\nu}$. The nucleus emits both particles through an inelastic collision that conserves linear momentum, and both particles share the energy and momentum neglecting the nuclear recoil (of order of few eV) as shown in Figure 1.2.[4]

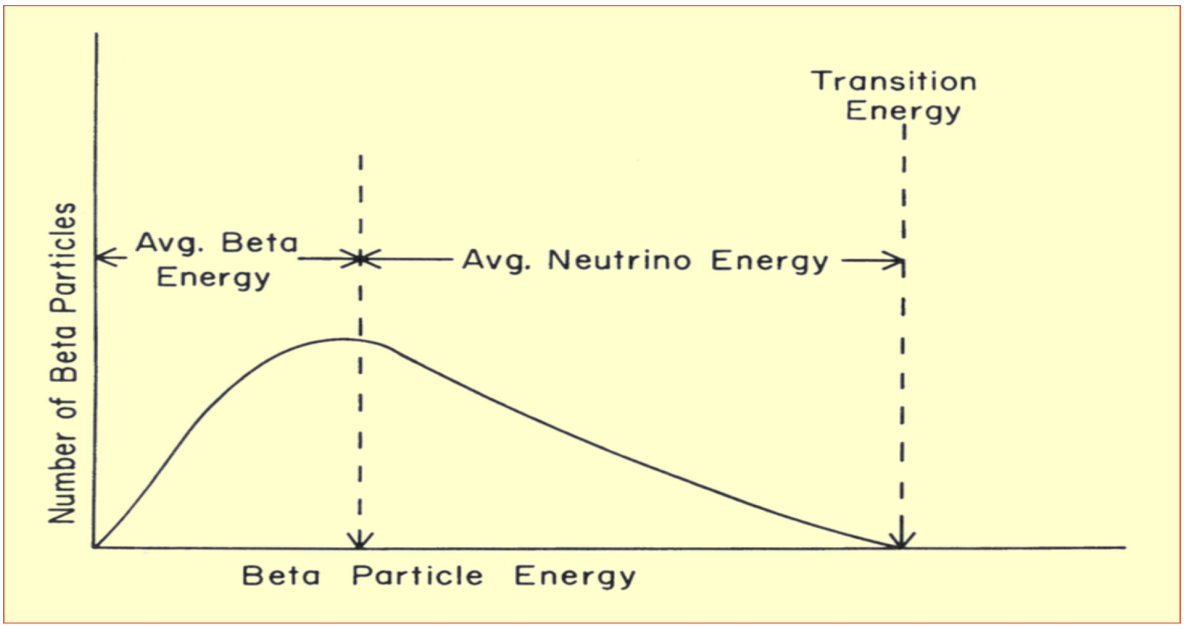

Figure 1.2: β^--particle and $\bar{\nu}$ energy spectrum.

1.1.3 Internal Conversion and Auger Electrons

Internal conversion and Auger electrons are similar interactions in that both of them emit electrons along with photons. Nevertheless, the beginning of each interaction is different. In internal conversion, atomic electrons absorb the excited energy of the nucleus which is emitted mostly as γ-rays. The electron energy is less than that of the emitted γ-rays since the difference in energy is used in releasing the electron from the atom. On the other hand, Auger electrons are released after absorbing part of the emitted X-rays from the electron cascade when the electrons fill the vacancies after an electron capture by the nucleus. Therefore, the outcomes of the two processes are similar in that they both produce electrons and photons as X-rays and γ-rays.

Besides the fact that the internal conversion and Auger electrons start differently, there is a difference in the emitted X-ray spectra for these processes. In internal conversion, the irradiated X-rays from the atomic electron cascade is higher in energy compared

to those emitted from the Auger electrons.[4] However, the irradiated γ-rays depend on the state of the mother and the daughter nuclei as will be shown in the next section.

Both U-233 and Th-232 emit electrons by internal conversion and Auger electrons; their average energy is 5.043 keV for U-233 and 11.82 keV for Th-232. The internal conversion and Auger electrons of these radioisotopes are lower in energy compared to the energy of the emitted β-particles from Pa-233.[4]

1.1.4 γ-Particles Emission

γ-emission occurs when a unstable nucleus transitions from an excited state to a lower excited state or to the ground state. The emitted γ-particle energy depends on the difference between the initial and final nuclear energy state of the daughter nucleus. When the unstable nucleus emits γ-particles, they isotropically spread them in the surrounding medium to interact with its atoms and molecules by photo-absorption, Compton scattering, or pair production. Figure 1.3 shows the photo-absorption and incoherent scattering cross sections for 90/10 Ar/CO_2 gas.[5]

γ-emission usually is emitted with other radioactive decays such as α-decay and β-decay depending on the final state of the daughter nucleus. If daughter nucleus occupies an excited nuclear state after an α or a β-decay, it will emit γ-rays as mentioned previously in section Section 1.1.2. However, if the daughter nucleus directly occupies the ground state after the radioactive decay, it will ban any further γ-emission.[4] In this work, the detector has a U-233 coating, and none of the radioactive nuclei has the ground state as the final nuclear state during any α or β-decay.

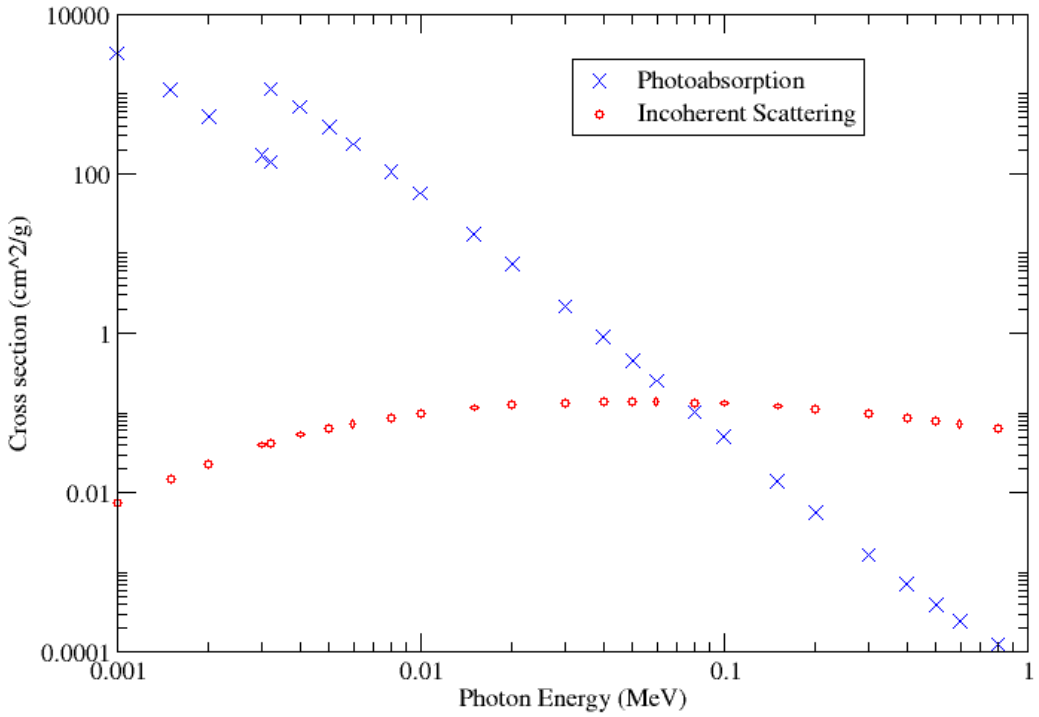

Figure 1.3: Photo-absorption and incoherent scattering cross sections for 90% Ar-gas 10% CO_2 gas mixture.[5]

A HP-Ge detector measured γ-emission from U-233 coating. The results showed a very low emission that could be considered negligible. In addition, the gain of the GEM detector is set to avoid detecting any of those gammas. Therefore, γ-emission was negligible during all the detector's signal measurements and analysis. Needless to say, the γ-rays effect on the detector's signal may not be negligible during the detector exposure to a neutron flux. More details about γ-particle ionization and their simulations will be discussed in Chapter 4.

1.2 Energy Loss of Ions in Gases

1.2.1 Energy Loss of Heavily Charged Ion

The energy loss is a change in energy of a heavily charged particle when it reaches the closest distance to a nucleus. The effect Coulomb's force will cause a deviation in the track of the incident particle along with a change in its momentum. Studying the energy loss for heavy ions is simpler than studying the energy loss of electrons since heavy ions are hardly deflected and do not have multiple small-angle scattering.[6]

Bethe-Bloch equation calculates the theoretical energy loss for charged particles in the moderate relativistic energy range and is suitable for calculating the energy loss for fission fragments and α-particles. The energy loss for heavy ions is mainly dependent on the ion's velocity and its effective charge. This makes it different from the electron as shown in Equation 1.9. Thus, the energy loss for an ion will be similar to that of an electron of the same velocity if the energy loss is scaled to the effective charge of the ion.[6]

$$-\frac{dE}{dx} = \mathcal{K}z^2\frac{Z}{A}\frac{1}{\beta^2}\left[\frac{1}{2}\ln\left(\frac{2m_ec^2\beta^2\gamma^2}{I}\frac{T_{max}}{I}\right) - \beta^2 - \frac{\delta}{2}\right] \tag{1.9}$$

$$T_{max} = \frac{2m_ec^2\beta^2\gamma^2}{1 + \frac{2\gamma m_e}{M} + (\frac{m_e}{M})^2} \tag{1.10}$$

$$\frac{\mathcal{K}}{A} = \frac{4\pi N r_e^2 m_e c^2}{A} = 0.307075 MeV g^{-1} cm^2 \tag{1.11}$$

The maximum kinetic energy is defined by Equation 1.10, where α is the fine structure constant ($\alpha = e^2/4\pi\epsilon_0\hbar c$), M is the incident particle mass in MeV/c^2, E is the incident particle energy γMc^2 in MeV, T is the kinetic energy in MeV, m_ec^2 is the rest mass of the electron (m_ec^2 =0.51 MeV), r_e is the classical electron radius ($r_e = e^2/4\pi\epsilon_0 m_ec^2 = 2.8fm$), N_A is Avogadro's number ($N_A = 6.022 \times 10^{23} mol^{-1}$), z_e is the charge of the incident particle, Z is the atomic number of the absorber, A is the atomic mass of absorber

in g/mol, I is the mean excitation energy in eV, $\delta(\beta\gamma)$ is the density effect correction to the ionization energy loss, and N is the electron density in unit of r_e^{-3}.

When the heavy ions pass through a medium, the maximum energy transfer to the medium is calculated using Equation 1.10. However, for heavy ions with a non-relativistic velocity of $\gamma \to 1$ and $2\frac{m_p}{M}\gamma << 1$, Equation 1.10 can be written as shown in Equation 1.12.[6]

$$T_{max} = \frac{2m_i c^2\beta^2\gamma^2}{1 + 2\gamma r + r^2} = 4E\frac{m_p}{M}\left(1 + \frac{E}{2m_p c^2}\right) \tag{1.12}$$

where $r = \frac{m_p}{M}$, and m_i and E are the mass and the energy of the heavy ion. If the ions are identical, T_{max} = E, then the amount of energy transfer reaches E/2.[6]

The density effect and the shell corrections in Equation 1.9 are negligible for heavy ions. The passage of heavy ions in a material with an energy of order 1-2 MeV/amu do not affect the material dielectric constant, especially if the medium has high Z materials and the velocity of the heavy ion is larger than that of the electrons in the atomic inner shells. Therefore, as far as the energy loss for the emitted α-particles and fission fragments from U-233 is concerned, these two corrections are negligible.

However, there are other corrections that affect the heavy ions' stopping power: Born approximation, Barkas' correction, and Bloch's correction. The corrections for the stopping power appear when the stopping number is expanded as shown in Equation 1.13. Thus, Bethe-Bloch's equation can be written as shown by Equation 1.14 as a first order approximation.[6]

$$L = L_0 + ZL_1 + Z^2L_2 \tag{1.13}$$

$$\frac{dE}{dx} = \frac{4\pi z^2 e^4 Z}{mv^2} N L_0 \tag{1.14}$$

$$L_0 = \frac{1}{2}\ln\left(\frac{2m_e c^2\beta^2\gamma^2}{I}\frac{T_{max}}{I}\right) - \beta^2 - \frac{\delta}{2} = \ln\frac{2mc^2\beta^2\gamma^2}{I} - \beta^2 - \frac{c}{Z} - \frac{\delta}{2} \tag{1.15}$$

In Equation 1.15, L_0 is the stopping number that is derived from Born approximation, and defined originally by Equation 1.9. L_1 is Barkas' correction, L_2 is Bloch's correction, and Z is the heavy ion atomic number.

Both Barkas' and Bloch's corrections are important for low energy ions such as fission fragments. Barkas' correction considers the little difference between the stopping power for positive and negative ions, which is effective for targets that have high-Z and low energy such as the emitted fission fragments from U-233 coating. Additionally, Bloch's correction calculates the effect on the stopping power for the ion when its velocity becomes lower than that of the electrons in the inner shells for the target atoms and molecules. Using these corrections, the stopping power can be written as in Equation 1.16.[6]

$$\frac{dE}{dx} = \frac{4\pi z^2 e^4 Z}{mv^2} NL \tag{1.16}$$

Finally, the highly charged ions have a charge exchange with the target composites and this charge does not always equal Z. When the highly charged ions pass through the medium, electrons leave and attach to the projectile ion. An average charge for the ion was be described using Equation 1.17.[6]

$$Z_{eff} = \left[1 - \exp\left(-\frac{v}{v_0 Z^{2/3}}\right)\right] Z \tag{1.17}$$

Therefore, the final form of the Bethe-Bloch's equation for the highly charged ions can be written using the correction for the stopping number in Equation 1.13, and dividing Equation 1.16 by Z_{eff}^2 from Equation 1.17 as a function of velocity with L_1 and L_2 corrections as shown in Equation 1.18.[6]

$$\left(\frac{dE}{dx}\right)_{scaled} = \frac{dE/dx}{Z_{eff}^2} = \frac{4\pi e^4 Z}{mv^2} NL \tag{1.18}$$

Simulation packages calculate the energy loss with specific uncertainties when a charged particle passes through a target material. GEANT4[7] and Srim & Trim[8] estimate the energy loss for different media. Nevertheless, the uncertainty of STRIM &

TRIM calculations in the gaseous media may reach 20%. The two types of calculations will be illustrated in the simulation and analysis chapter.

The energy loss of heavily charged ions releases free electrons that lose their energy in the surrounding medium. When the energy loss of the charged particles transfers to the medium through elastic and inelastic collisions, the incident ion either ionizes or excites atoms and molecules in the surrounding medium and exchanges charges with the medium's composites. Therefore, the passage of the heavily charged ions produces free electrons which could interact with the medium's composites again as will be discussed in detail in the next section.

1.2.2 Electron Stopping Power

The electron loses its energy either by collision, radiation, or both depending on the energy of the electron and the surrounding medium. When the electron interacts with the surrounding medium, the energy transfers to the medium as shown in Equation 1.19. If the electron is in the non-relativistic energy range, most of its energy transfers to the medium by collisions. On the other hand, the electron could lose its energy by radiation depending on the medium composites. If the atomic number of the medium is larger than 80, then the minimum energy of incident electrons will be at least 10 MeV to loss energy by radiation (Bremsstrahlung).[6]

$$\left(\frac{dE}{dx}\right)_{total} = \left(\frac{dE}{dx}\right)_{collision} + \left(\frac{dE}{dx}\right)_{radiation} \tag{1.19}$$

The mean stopping power formula estimates the incident β-particles and free electron energy loss by collision. The Bethe-Bloch equation is used to estimate the electron stopping power that is shown in Equation 1.20. It is simplified due to the gaseous medium properties and to the expected energy range of the electrons that interact with gaseous medium.[6]

$$\frac{dE}{dx} = \frac{2\pi N z^2 e^4}{mv^2}\left(\ln\frac{(\gamma+1)E^2}{2I^2} - (\frac{2}{\gamma} - \frac{1}{\gamma^2})\ln 2 + \frac{1}{\gamma^2} + \frac{1}{8}(1-\frac{1}{\gamma})^2 - \delta\right) \tag{1.20}$$

As to non-relativistic electrons, such as those emitted from a U-233 source as β-particles and free electrons produced by ionization, they have $\gamma \to 1$ $\delta \to 0$, and the density effect is negligible for gases due to the low density N. Equation 1.20 is simplified to Equation 1.21.

$$\frac{dE}{dx} = \frac{2\pi N z^2 e^4}{mv^2}\left(\ln\frac{E^2}{I^2} - \ln 2 + 1\right) \tag{1.21}$$

Thus, the stopping power for electrons is almost the same for all gases under the same temperature and pressure, and the amount of energy loss is dependent on the inverse of the squared velocity of the electron. Additionally, Equation 1.21 does not consider the effect of the electric field that accelerates the free electrons in gas as it will be demonstrated in detail in Section 1.3.4.

1.3 Charged Particles Transport and Ionization

Studying diffusion and mobility of charged particles in a gas is classified into two main groups, ion and electron diffusion and mobility. They are conceptually similar, but they have many differences. First, the ratio between the mass of the electrons and the gas atoms is very small, so with a few eV of work done by an electric field, the electrons will gain a high velocity compared to ions that are accelerated under the same electric field.[9] Also, the probability of low energy electrons to interact is higher than that of low energy ions, and the electron interactions are supported with accurate calculations for the electron drift velocity. Electrons at a low energy have the ability to produce vibrations and excitations in the gas atoms or molecules which are measured within the lab frame, but low energy ions have very low cross sections for most of the interactions for most of these interactions.[9] When interactions occur, a complexity appears in measuring the products of ion interactions. Nevertheless, the calculations are simpler for the velocity distribution of electrons in many gases since the ratio between a gas atom or molecule mass to the electron mass is very small.[9]

Since producing electrons is simpler than producing ions in a gas, many interactions are responsible for producing electrons, such as thermionic emission, photo-emission, or radioactive decay. On the other hand, creating an ion requires electron bombardment, photo-ionization or electric discharge, which requires more sophisticated conditions for the experiment. In addition, ions are not as sensitive as electrons for the non-uniformity of electric and the magnetic fields.[9] Finally, the existence of impurities in a gas is always a concern. The ions lose most of their energy at the molecular level, but the electron energy loss is within the atomic level in a pure gas. As a result, the ionic velocity distribution is not affected by the existence of these impurities except for some cases that are related to highly accurate ionic studies in gases.[9]

As to ionization, it is the dominant interaction for non-relativistic electrons and ions in a gaseous medium. Ionization occurs when the energy of charged particle is larger than

the ionization potential or the minimum energy to produce an ion-electron pair in the gas. If a charged particle moves under an electric field effect, this will accelerate the charged particle and increase its kinetic energy to ionize the surrounding gas. However, high energy ionizing particles are not effective in ionization since the ionization cross section in a gaseous medium is inversely proportional to the kinetic energy of the charged particle.

1.3.1 Charged Particle Drift and Diffusion

The motion of a charged particle in a medium is controlled by the magnitude and the direction of a drift electric field. The charge of a particle determines its velocity and direction when it moves under the electric field effect. In a system of identical particles, the particles move with the same direction as that of the electric field that will accelerates them, or in the opposite direction of the electric field which will decelerates them. Equation 1.22 and 1.23 represent the gain and the loss for each case. The total work of the electric field on an identical particle system is mv_d^2, where v_d is the drift velocity, and m is the mass of the charged particle as shown in Equation 1.24.[10]

$$\Delta\epsilon_p = \frac{m(v+v_d)^2}{2} - \frac{mv^2}{2} = mvv_d + \frac{mv_d^2}{2} \tag{1.22}$$

$$\Delta\epsilon_a = \frac{m(-v-v_d)^2}{2} - \frac{m(-v)^2}{2} = -mvv_d + \frac{mv_d^2}{2} \tag{1.23}$$

$$\Delta E = \Delta\epsilon_p + \Delta\epsilon_a = mv_d^2 \tag{1.24}$$

Additionally, the kinetic energy of a system of identical particles will fluctuate depending the drift electric field. If the average energy of a charged particle is $\bar{\epsilon} = \frac{m\bar{v}^2}{2}$, the fluctuation in its kinetic energy will be proportional to the average velocity of the charged particle $\bar{v}$ and its drift velocity v_d when the charged particle moves with v_d in a uniform electric field as shown in Equation 1.25.[10]

$$\frac{\Delta E}{\bar{\epsilon}} = \frac{m v_d^2}{\frac{m\bar{v}^2}{2}} \sim \left(\frac{v_d}{\bar{v}}\right)^2 \tag{1.25}$$

1.3.2 Electron Drift and Diffusion

In a gaseous medium, electron density is dependent on the gas mobility and diffusion coefficient when electrons move in the medium. If an electron flux is defined as in Equation 1.26, the continuity equation describes the relationship between the rate of the electron density and the electron flux as shown in Equation 1.27, where q is a source of charge creation or annihilation in $cm^3 s^{-1}$. Not only is the average velocity of the electron constant in the previous equations, but so are the mobility and the diffusion coefficients for a medium of a constant temperature and pressure.[10]

$$\Gamma = \pm n\mu E - D\nabla n \tag{1.26}$$

$$\frac{\partial n}{\partial t} + \nabla.\Gamma = q \tag{1.27}$$

However, estimating the change in electron density using the continuity equation is imperfect since the assumption in these equations is that all the electrons have an identical transition in the macroscopic quantities of the gaseous medium, such as the dielectric constant and the conductivity, which approximates the values of these macroscopic quantities. To accurately analyze the microscopic processes, such as ionization and atomic excitation, the electron distribution function $f(r, v, t)$ should be defined using the Boltzmann transport equation.[10]

1.3.3 Heavily Charged Ion Ionization

The major interaction of the charged particles in a fission chamber is the ionization of Ar/CO_2 gas. Before operating a fission chamber, the air inside is flushed and replaced with 90/10 Ar/CO_2 to increase the probability of ionization by an incident charged particle.

Generally, the ionization cross section for air is smaller than the one for Ar/CO_2 gas or any inert gas mixtures.

A heavily charged ion produces ion-electron pairs when the ion ionizes a gaseous medium. The number of ion-electron pairs produced by ionization is directly proportional to the incident ion energy. Through out the ion's passage, its kinetic energy decreases because it exchanges its charge with the medium atoms and molecules. The charge exchange decreases the number of free electrons as the incident ion is transported further in the region of the drift electric field. The number of free electrons can be calculated using the mean ionization energy to create an electron-ion pair and the energy loss of the incident ion in the medium as shown in Equation 1.28, where N is the number of incident ions, and W is the mean ionization energy for the target, which equals on average 26 eV for 90/10 Ar/CO_2 gas mixture.[11]

$$Q = N \times \frac{(dE/dx)}{W} \tag{1.28}$$

However, the assumption in Equation 1.28 is that ion energy loss in the gaseous medium is completely for ionization without considering any other processes such as atomic excitations and molecular vibrations. These latter two interactions were in fact involved when GEANT4 simulated the ion transport in the gas as will be discussed in Chapter 3.

1.3.4 Electron Ionization and Multiplication

It was experimentally observed that applying a voltage difference on a gas cavity produces a current. Townsend observed a number of electrons produced by a uniform electric field which was created by applying a voltage V on a gas cavity.[12] If the number of electrons n_0 travels a distance d in a gas, the number of the electrons, after passing the distance d, is calculated using Equation 1.29, where α is The Townsendfirst coefficient. However, The Townsendfirst coefficient specifies photo-ionization and electron collision with gas atoms

and molecules as major processes for electron multiplication, ignoring the other processes such as electron reattachment, electron scattering, and molecular excitations.[12]

$$n = n_0 e^{\alpha d} \tag{1.29}$$

Townsend studied the relationship between the Townsend first coefficient α and the applied electric field E. Townsend accurately predicted all the values of α for different values of E using Equation 1.30, where p is the gas pressure, A and B are constants that are dependent on E and the gas thermal characteristics. Nevertheless, having a single analytical function to fit the experimental results for a gas does not exist because α/p is dependent on the number of produced electrons, and this number changes when the average energy distribution of the ionizing electrons changes.[12]

$$\frac{\alpha}{p} = Ae^{(\frac{-Bp}{E})} \tag{1.30}$$

Besides the previous method, α/p could be calculated depending on the mean free path of ionization using Equation 1.31 which defines the average mean free path λ, where σ_i is the ionization cross section, and x is the distance traveled by an electron in a gas. Substituting the value of λ from Equation 1.31 results in redefining A and B in terms of the ionization cross section as shown in Equation 1.34.[12]

$$\bar{\lambda} = \frac{kT}{p\sigma_i} \tag{1.31}$$

$$\alpha = -\frac{f'(x)}{dx} = 1/\bar{\lambda}e^{\lambda_i/\bar{\lambda}} \quad f'(x) = e^{-x/\bar{\lambda}} \tag{1.32}$$

$$\frac{\alpha}{p} = \frac{\sigma_i}{kT}e^{-\sigma_i/kT(V_i/(E/p))} = Ae^{-B/(E/T)} \tag{1.33}$$

$$A = \frac{\sigma_i}{kT} \quad B = \frac{\sigma_i V i}{kT} \tag{1.34}$$

Percentage of CO_2	A $(cm^{-1}Torr^{-1})$	B $(Vcm^{-1}Torr^{-1})$	$\frac{E}{p}$ $(Vcm^{-1}Torr^{-1})$
3.7	5.04	90.82	16.2
2.8	221.1	207.6	21.6
87.2	158.3	291.8	32.9
100	145.1	318.2	36.4

Table 1.2: A and B measured values for different Ar-gas and CO_2 gas mixtures.[13]

The Townsend ionization coefficient is directly proportional to the applied electric field. Figure 1.4 shows the ionization coefficient for both Ar and CO_2 gases. Ar gas has a larger Townsend coefficient for a specific value of E/p than CO_2 gas does due to other processes that could occur in CO_2 gas besides ionization, as will be discussed in Section 1.3.5. Consequently, mixing the two gases decreases the number of free electrons that are liberated during electron multiplication. Table 1.2 shows different values for A and B when CO_2 gas when the mixing percentage is changed along with $\frac{E}{p}$.

However, the more accurate method to calculate electron multiplication is by solving the Boltzmann equation. The Boltzmann equation defines a velocity distribution for primary electrons when they are produced by the energy loss of the incident particles. The velocity distribution is dependent on the electrons' kinetic energy, electric field, and gas transport properties such as drift velocity and diffusion coefficients. Additionally, the velocity distribution in phase space is the appropriate method to study the effect of microscopic processes, such as electron ionization and reattachment.[12]

If f is a distribution function of electron velocity in a gaseous medium, then the Maxwell Boltzmann differential equation is written as shown by Equation 1.35, where n is the number electrons propagating in the presence of an electric field E, c is the velocity of the electrons, and S depends on the elastic and inelastic collision cross sections of the medium.[14]

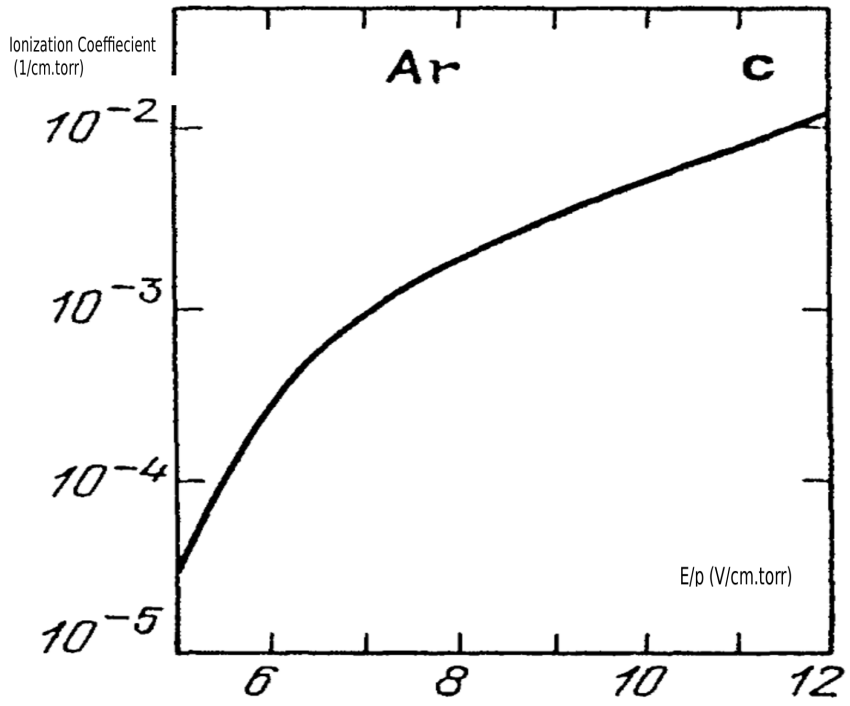

(a)

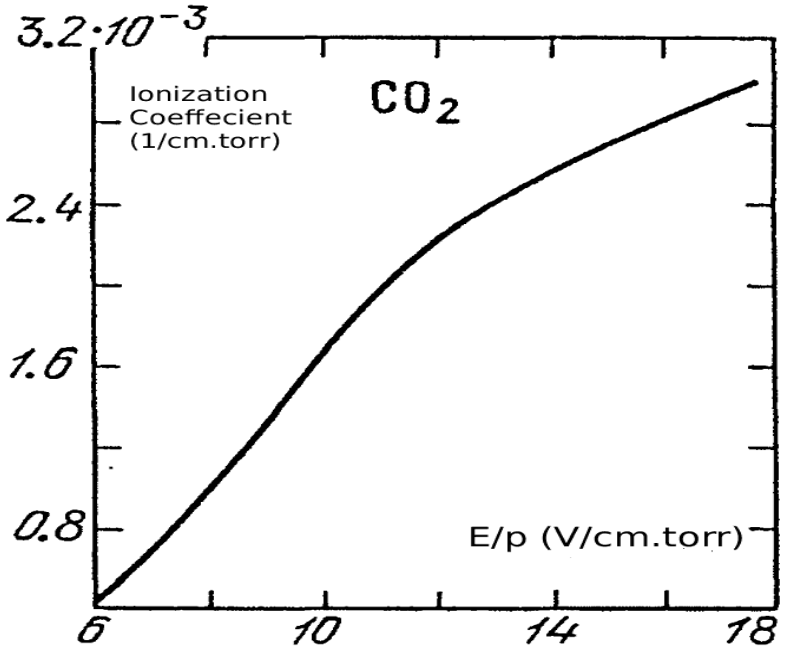

(b)

Figure 1.4: Electric field in unit of V/cm.torr and the ionization coefficient α/p in unit of $cm^{-1}.torr^{-1}$ for (a) Ar-gas. (b)CO_2 gas.[10]

$$\frac{\partial}{\partial t}(nf) + \nabla_{.r}(nfv) + \nabla_{.v}\left(nf\frac{eE}{m}\right) + S = 0 \tag{1.35}$$

The equation includes the loss of electrons as they transport across a surface boundary in a volume element **dr**, and the effect of a uniform electric field in accelerating each n**dr** electron which changes their velocity dc from one point to another in the phase space, and the loss in the number of points in a time dt is $dt\nabla_{.v}(\frac{nfeE}{m})dv$**dr**. The loss in the electron density Δn in dv is as a result of a quasi discontinuous change in a position Δv in velocity space as each electron attached to an ion.[14] The solution of the Boltzmann equation in 3D-space for an electron traveling toward the z-axis under a uniform electric field is represented by Equation 1.36, where r' is defined as shown in Equation 1.37.[14]

$$n(x, y, z) = \frac{i}{(4\pi D)}\frac{\exp^{\lambda(r'-z)}}{r'}, \tag{1.36}$$

$$r' = (z^2 + \frac{D_L}{D}\rho^2)^{1/2} \tag{1.37}$$

The asymtotic solution for a stream of electrons originating from a hole in a metal plate extends over a plane at z=0, and has a hole at the origin. The Scalar Boltzmann equation can be written for an electron stream moving in the +z-direction, as shown in Equation 1.38 taking into consideration all the conditions mentioned previously and having S = 0, the general solution for Equation 1.38 is shown in Equation 1.39. [14]

$$D\left(\frac{\partial^2}{\partial x^2} + \frac{\partial^2}{\partial x^2}\right)n + D_L\frac{\partial^2}{\partial z^2} - W\frac{\partial}{\partial z}n = 0 \tag{1.38}$$

$$n = e^{\lambda_L z}\sum_{k=0}^{\infty} A_k r'^{-1/2} K_{k+1/2}(\lambda_L r')P_k(\mu) \tag{1.39}$$

where $r'^2 = \sqrt{x'^2 + y'^2 + z'^2}$, with $x' = (\frac{D_L}{D})^{1/2}x$, $y' = (\frac{D_L}{D})^{1/2}y$, $2\lambda = \frac{W}{D_L}$, K_m is modified Bessel function, and $\mu = cos\theta$. More details about the solution in Equation 1.39 is provided in Appendix A.1.

However, for an electron stream traveling toward +z axis in a uniform electric field, the velocity distribution has only two terms $f_0 + f_1$ which are for a monopole and dipole solution as shown in Equation 1.40 and Equation 1.41. These solutions are only applicable for a constant electric field inside the hole. These solutions can be used to estimate the change in the electron density for specific values of an electric field inside the hole.[14] On the other hand, Garfield simulation solves the Boltzmann equation by using Magboltz package with a variable electric field, as will be discussed in simulating the electron multiplication by GEM preamplifiers. [15][16]

$$n_{monopole} = (\frac{\pi}{2\lambda_L})^{1/2} \frac{e^{-\lambda_L(r'-z)}}{r'} \tag{1.40}$$

$$n_{dipole} = (\frac{\pi}{2\lambda_L})^{1/2} \frac{z}{r'}(1 + \frac{1}{\lambda_L r'}) \frac{e^{-\lambda_L(r'-z)}}{r'} \tag{1.41}$$

$$r' = \sqrt{\rho'^2 + z^2} \tag{1.42}$$

1.3.5 Gas Quenching

Gas quenching is mixing gases to embed non-ionizing processes such as molecular excitation and vibration which decreases the energy of a charged particle to create ionization. The gas mixture consists mostly of one gas whose atoms are the main source of electrons along with another molecular gas which decreases the number of free electrons in the gaseous medium. In other words, the probability for ionizing the atoms in the gas mixture decreases due to the electron interaction with the quenching gas molecules by the molecular excitations and vibrations that are shown in Table 1.3. Consequently, a higher voltage is required to get a gain from this gas mixture than a medium which only has a non-quenching gas.[17]

The quenching process not only decreases the ionizing electron energy, but also decreases the energy positive ions (produced by ionization) when the ions collide with

$e + CO^+ \rightarrow$	$CO_2^+ + 2e$	Single Ionization
	$C + O^+ + e$	Dissociative Excitation
	$C^+ + O + e$	Dissociative Excitation
	$C^+ + O^+ + 2e$	Dissociative Ionization

Table 1.3: CO_2 gas electron interactions besides ionization.

these gas molecules. In the case of Ar gas, quenching emits one or more photons from these positive ions which represents an energy loss in a form other than the ionization.This effect is known as an argon escape peak.[17]

Mixing Ar gas with another organic gas such as CO_2 decreases the number of secondary electrons. Producing an ion-electron pair in pure Ar gas requires 15.75 eV. However, after quenching with an organic gas such as CO_2 gas at 9:1 ratio, the quenching increases the mean energy required for producing an ion-electron pair to 26 eV on average for most of the incident charged particles. As a result, the number of free electrons decreases through the passage of the charged particle through the 90/10 Ar/CO_2 gas mixture.[18]

Chapter 2

Apparatus

The detector was an ionization chamber which then used to detect the emitted ions from the U-233 coating on a cathode plate in Ar/CO_2 gas mixture. The ionization chamber consisted of a cathode plate followed by three GEM preamplifiers and a segmented anode plate to collect free electrons transported by an electric field created by a voltage difference applied between the cathode and the anode. The GEM preamplifiers established an electric field to accelerate the free electrons when they passed through one of holes on its surface and created secondary electrons. Secondary electrons avalanche after multiplication was collected by the segmented anode. The detector cavity, made of ertalyte, contained all of the components and isolated them from the surrounding atmosphere. A high voltage divider circuit was used to operate the detector and pass the detector signal through a high-pass filter to send it to the data acquisition (DAQ) system. This chapter discusses the detector construction and operation in detail.

2.1 GEM Detector Description

2.1.1 GEM Detector Assembly

As shown in Figure 2.1, the GEM detector was composed of a sealed cavity that contained three GEM preamplifiers, a cathode and a segmented anode. Before installing the GEM preamplifiers in the ionization chamber cavity, they were mounted on square fiberglass frames in a clean room environment. Then they were separated by a vertical distance of 2.8 mm using M3 washers inside the detector cavity parallel to each other. The cathode

plate had a vertical distance of 3.5 mm from the top of first GEM preamplifier. The segmented anode had a 1 mm distance from the last GEM preamplifier.

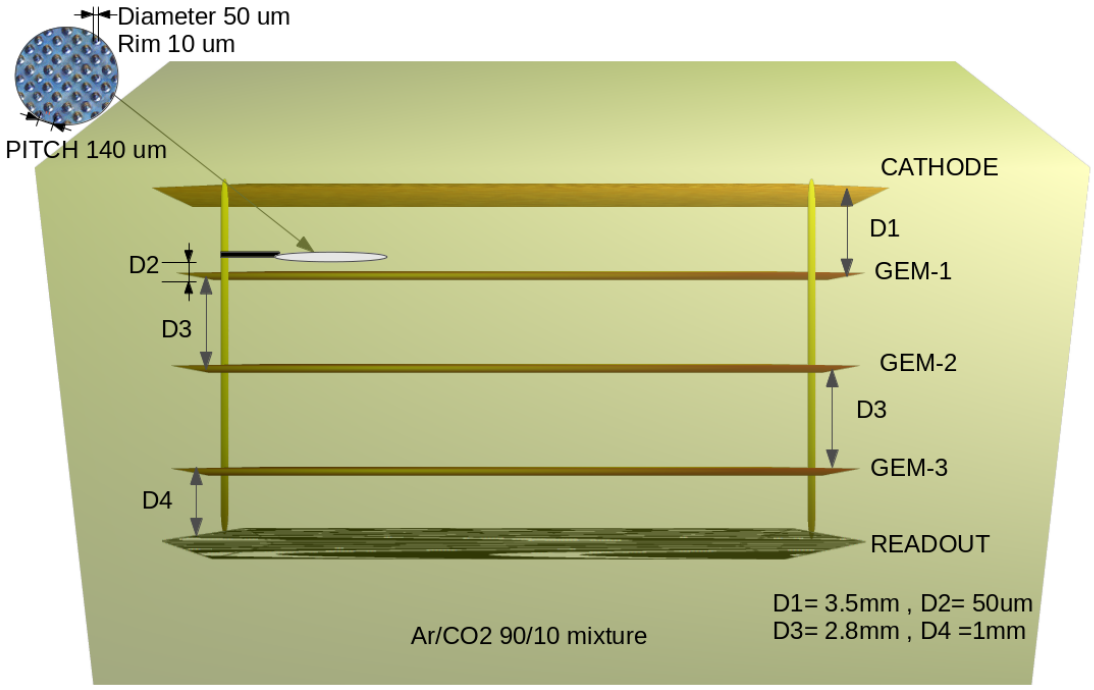

Figure 2.1: The original GEM detector design.

A 10x10 cm^2 cathode plate was built from a fiber glass copper clad plate which could hold a voltage difference up to 5 kV without any spark discharge. A 1 mm thick fiber glass copper clad plate was used as a cathode, and fiber glass layer helped to electrically isolate the copper layers when the voltage was applied. The cathode design was tested to hold a voltage of 5 kV (in air) between the top and bottom sides without any spark discharge.

The segmented anode was composed of thin strips made of copper that intersected with each other without being in contact. The charge collector was made of 50-80 micron wide strips that were isolated from each other in order to determine the location of the collected electrons. The strips were arranged to allow equal charge sharing on the upper

(x coordinate) and lower (y coordinate) intersecting layers of the charge collector as shown in Figure 2.2.[19]

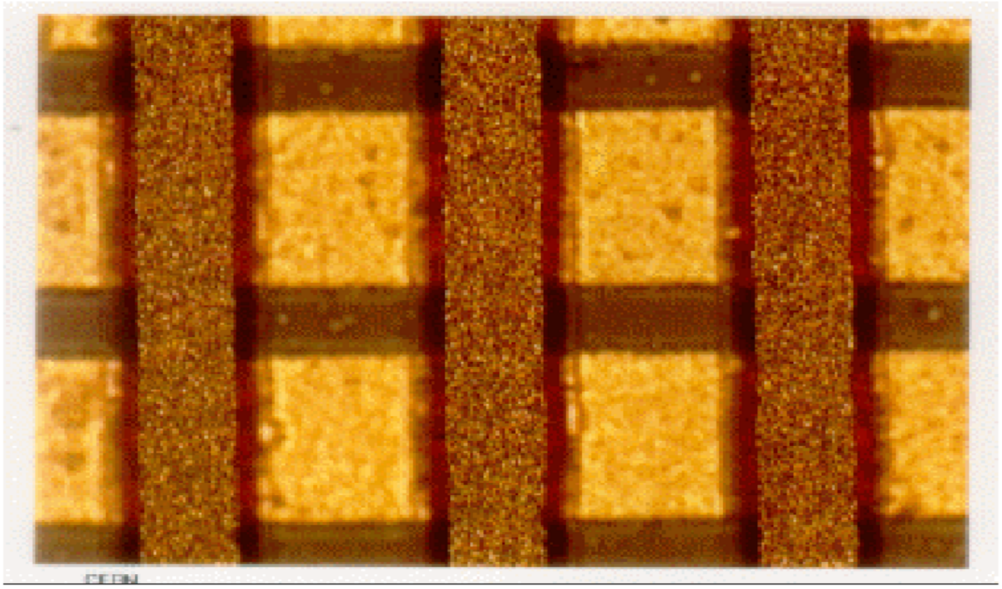

Figure 2.2: The charge collector 50 micron and 80 microns for horizontal and vertical strips successively.

Two machined plastic sheets, made of ertalyte, enclosed all the detector components inside a 2 cm thick sealed cavity. The two 1.25 cm thick ertalyte plastic sheets set on top of each other. they were machined to have a 13x13x2 cm^3 cavity. A 13x13x0.05 cm^3 kapton entrance window was built on the detector top to allow low energy range particles into the chamber. Additionally, the cavity was supported by an o-ring strip that was placed between the two plastic sheets and isolated the cavity after bolting the two sheets together with M3 plastic screws around the kapton window. Figure 2.3 shows top, bottom, and side views of the detector's exterior design.

The GEM preamplifiers were properly aligned allowing electron transport and multiplication. The chamber had three GEM preamplifiers with a separation distance of 2.8 mm, and they were properly aligned to achieve transparency to allow electron transport

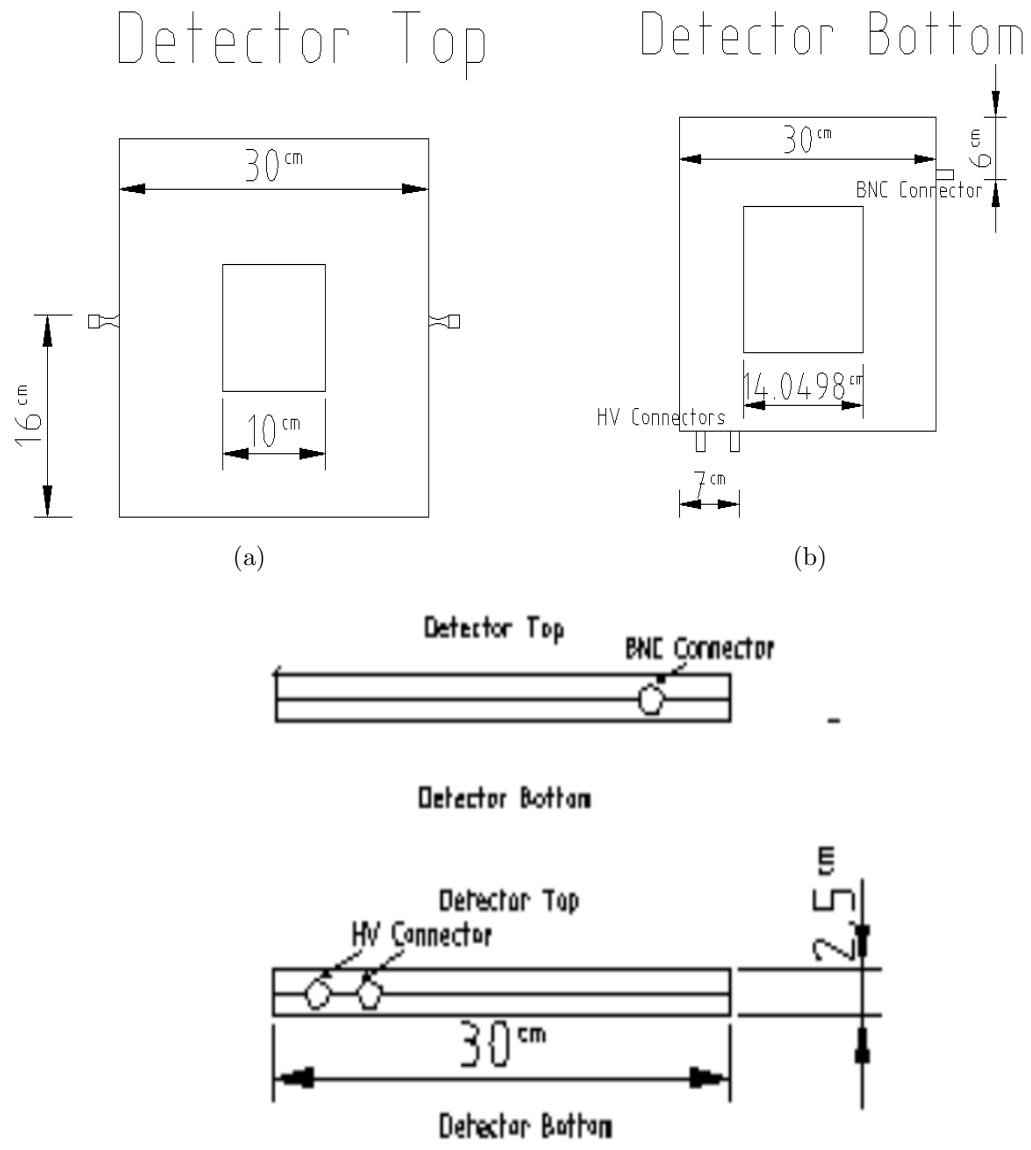

(a) (b)

(c)

Figure 2.3: The detector external structure (a) top view. (b) bottom view. (c) side view.

and three stages of multiplication. After setting voltage on each preamplifier, a signal was received from the detector which confirmed the appropriate alignment and separation distances for the GEM preamplifiers.

It is important to point out that the GEM design described above was not unique. GEM detectors differ in shape, area and number of the preamplifiers installed. The number of GEM preamlifiers varies depending on the required multiplication. For instance, a triple GEM design (gain of 10^6 electrons) provides an amplification suitable for imaging when using segmented readout plate. Moreover, the triple GEM is used for tracking low ionizing particles.[20]

Finally, the last advantage of using a triple-GEM design is the low spark discharge probability during the detector operation. The triple-GEM design has a gain of 10^6 electrons by applying low voltage on each preamplifier when is compared to applied voltage(s) on a single or a double GEM design. The lower voltage for the triple GEM design decreases the spark discharge probability and give a longer lifetime than the other GEM deigns. Figure 2.4 shows the gain and the spark discharge probability for the three GEM designs.[21]

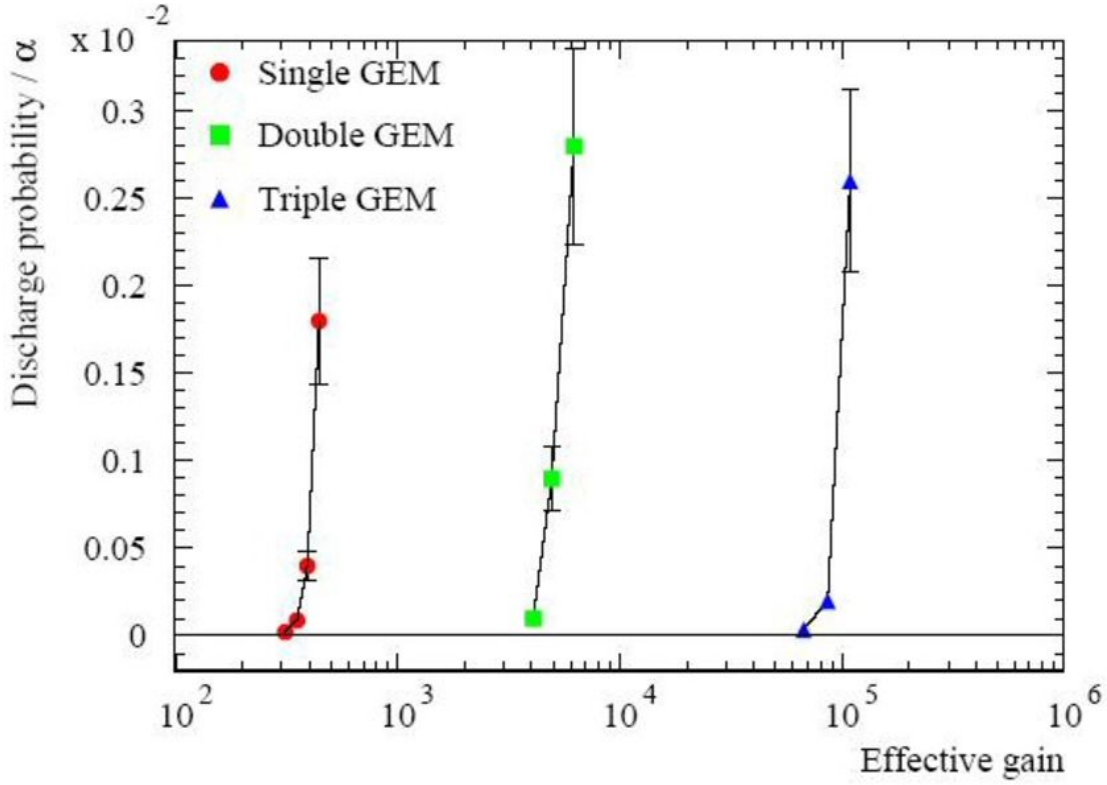

Figure 2.4: The probability of spark discharge for different GEM detector designs.

2.2 The Modified GEM Detector

The GEM detector was modified to be a fission chamber by installing a U-233 coating on the detector's cathode. The GEM detector design, as described in Section 2.1.1, was thus modified to be a neutron sensitive detector with this coating. The U-233 coating was installed on the cathode plate as a neutron sensitive material to mainly interact through a fission reaction with the incident neutron flux since it has a relative high cross section for the thermal and fast neutrons. The U-233 coating was placed to directly face the drift region of the GEM detector as shown in Figure 2.5.

In addition, the drift region was increased in height to increased the deposited energy from the heavily charged ions. The range of the heavily charged ions in a 90/10 Ar/CO_2

was 3.2 cm for 4.85 MeV α-particles. Therefore, the drift region was increased to 1 cm to increase the deposited energy of the incident α-particles to around 1 MeV. When the deposited charge by the ion increases, it decreases the required gain to observe the its signal which will be discussed in the coming chapters.

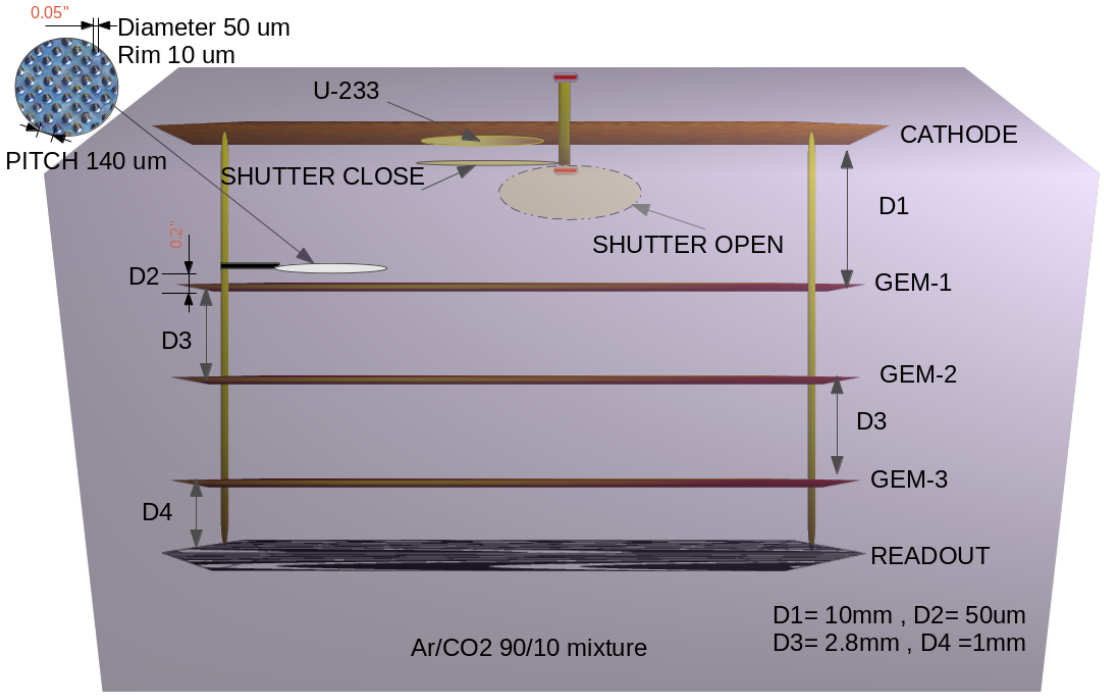

Figure 2.5: Modifications of the original triple GEM design to a fission chamber with a shutter.

The electroplated U-233 coating is a circular thin film of 2.5 cm diameter with a thickness of 30-40 μm carried on a circular metal plate that was attached to the detector cathode. Figure 2.6-b shows an 8 cm circular metal plate had the U-233 coating and helped in installing it on the detector cathode. The original cathode plate was machined to have a circular hole to make the coating directly be exposed to the drift region. Then an adhesive was applied to one side of the cathode to install the metal plate that has the U-233 coating as shown in Figure 2.6-b. The electrical contact between the two metal

plates was maintained during the installation to avoid any electrical spark discharge.

A circular fiber glass shutter, with a 2.5 cm diameter and 1 mm thickness, was designed to completely cover the U-233 coating, and it was manually opened or closed by the operator from outside the kapton window. This 1 mm thick fiber glass shutter was located 1.5 mm below the coating surface, and it covered the U-233 coating manually without turning of the detector using an extended rod from the end of the shutter to outside the kapton window. When the shutter was closed, it completely covered the U-233 coating. When the shutter was open, it exposed the U-233 coating to the drift region allowing the emitted particles from U-233 coating to ionize the gas. Figure 2.6-b and Figure 2.6-c show the cathode with open and closed shutter respectively.

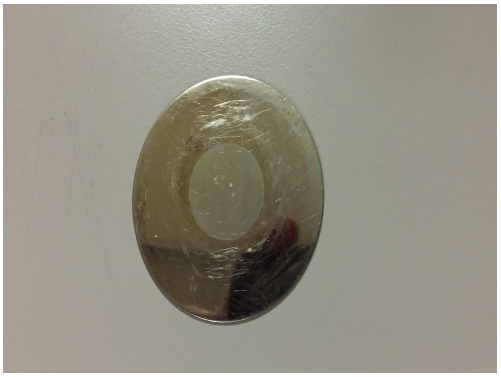

(a)

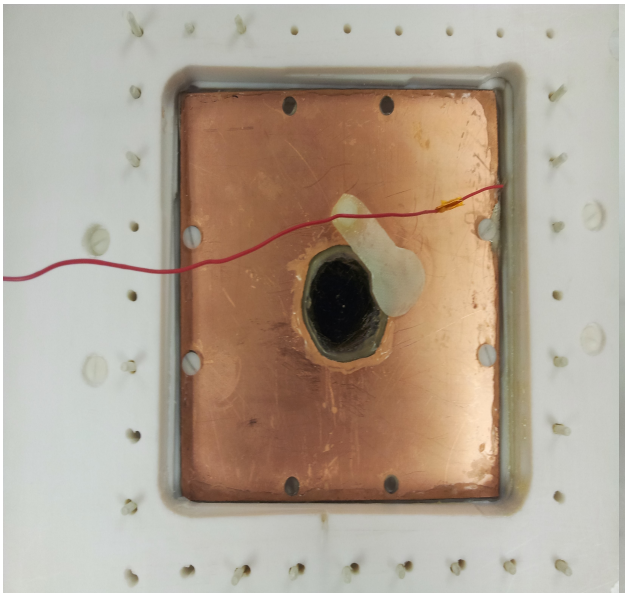

(b)

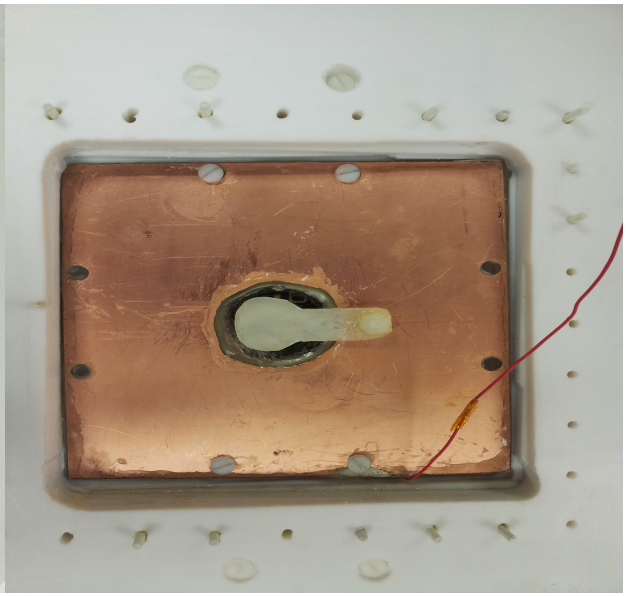

(c)

Figure 2.6: (a)The U-233 circular plate (b)The modified cathode with open shutter (c)and closed shutter.

Shutter position	α-particles Rate (min.$^{-1}$)
Open	6879
Closed	1

Table 2.1: α-particles rates for open and closed shutter.

The fiber glass shutter was tested to stop the emitted α-particles from U-233 coating. An alpha particle counter showed a difference in the number of the counted α-particles when the shutter was open and when it was closed as shown in Table 2.1.[22] Since the α-particles were stopped when the shutter was closed, all the fission fragments will be stopped that are emitted from the U-233 coating during the exposure to a neutron flux.

The height of the detector cavity was increased in order to have a larger drift region to contain the modifications. The height of the kapton window was changed to 1.5 cm from the first GEM preamplifier design which was 0.7 cm as shown in Figure 2.7. The increment in height helped in installing the modified cathode with the fiber glass shutter to provide the chamber with a 1 cm height drift region as shown in Figure 2.5.

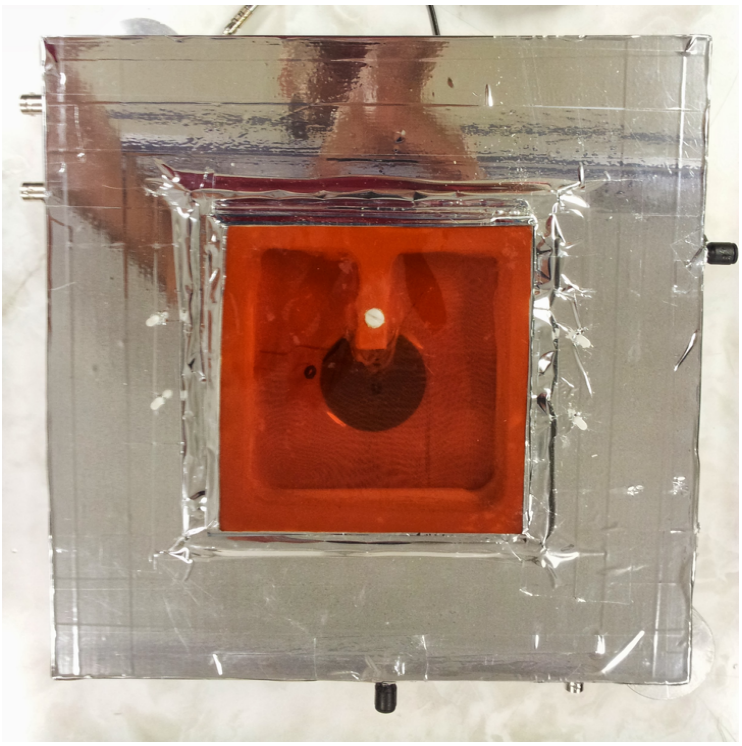

(a)

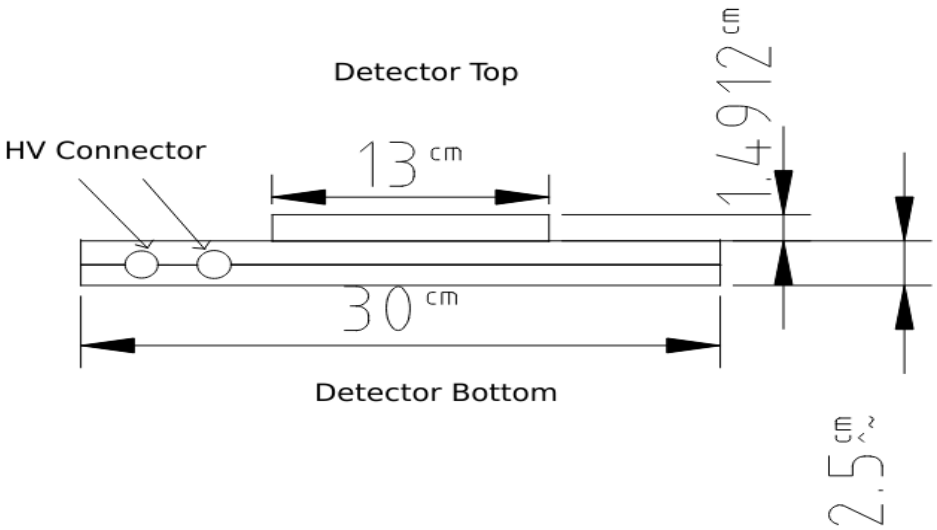

(b)

Figure 2.7: The detector external structure after modification (a) top view. (b)dimensions of the new cavity.

2.2.1 GEM Preamplifiers

A GEM preamplifier is a 50 micron thick kapton foil clad on both sides with 5 microns of copper. A staggered pattern of 50 micron diameter holes, equally spaced by distances comparable to the hole diameter, was chemically etched into the copper clad foil of a 140 um pitch distance over an area of 10x10 cm^2 as shown in Figure 2.8.[23] The advantage of using GEM preamplifiers is their ability to multiply electrons (preamplification). The structure, shape, and number of preamplifiers changes depending on the application. For instance, a single GEM preamplifier increases the number of liberated electrons by two orders of magnitude via electron multiplication. However, a triple GEM assembly increases the gain up to 10^6 electrons which is used mostly for imaging applications.[24] Operating the GEM preamplifiers requires installing them in a sealed chamber, as discussed in Section 2.1.1, and then providing them with voltage, as illustrated in the next section.

When the voltage is applied on the GEM preamplifier, it produces an electric field inside the holes which is the main component in the electron multiplication process. Figure 2.8 shows the electric field lines inside the holes whose number increases close to the edge of the hole. They are different designs for GEM preamplifiers that are different in the size or shape of the hole, or different in the size of the rim around each hole. The aim of those modifications is to increase the numbers of electric field lines and to study the effect of their curvature on the gain of the used preamplifier. Furthermore, GEM designs are used to study decreasing the spark discharge effect when in areas of high electric field by testing different materials for isolating and cladding.[25]

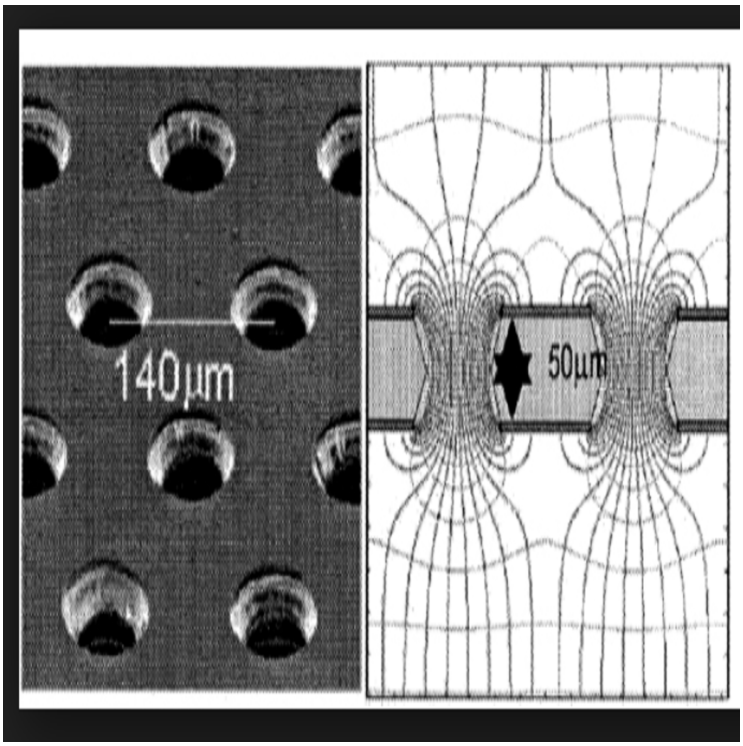

(a)

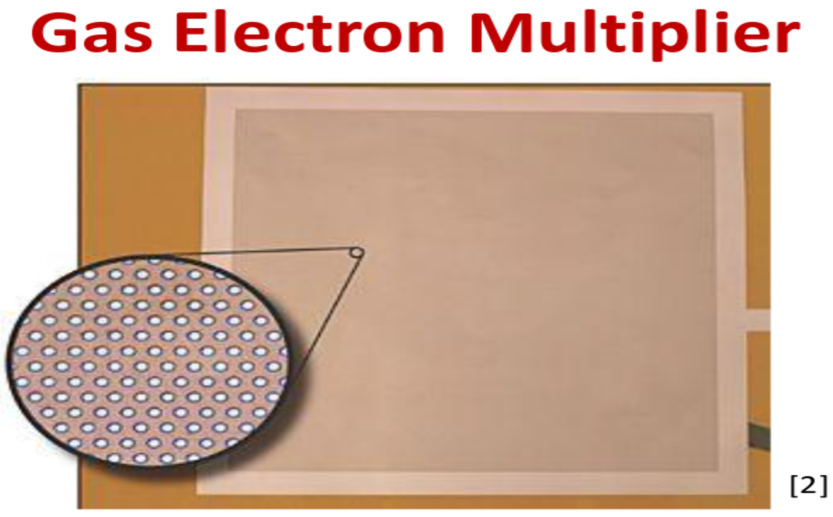

(b)

Figure 2.8: (a)The GEM preamplifier design with its electric field. (b) GEM preamplifier card.

2.3 High Voltage Divider Circuit

A high voltage divider circuit was used to apply a negative voltage between the top and the bottom sides of each GEM preamplifier. Figure 2.9 shows the components of the voltage divider circuit that provide negative voltages for each GEM preamplifier. It was designed to place the first GEM preamplifier encountered at the highest voltage difference between the top and the bottom sides while the last GEM preamplifier had the least voltage difference. The advantage of decreasing the voltage as the preamplifier became closer to the ground voltage was to avoid spark discharge during the detector operation. Figure 2.9 shows the high voltage circuit divider design [26], and Table 2.2 lists the voltage measured on each GEM preamplifier.

$V_{source} \pm 1$	2579	2630	2680	2731	2781	2832	2900	2933
$V_{G1T} \pm 1$	2579	2630	2680	2731	2781	2832	2900	2933
$V_{G1B} \pm 1$	2259	2303	2348	2393	2373	2482	2562	2591
$\Delta V_1 \pm 1$	304	310	316	322	328	332	338	342
$V_{G2T} \pm 1$	1671	1704	1737	1770	1803	1836	1880	1902
$V_{G2B} \pm 1$	1394	1421	1449	1476	1503	1530	1567	1585
$\Delta V_2 \pm 1$	279	285	290	296	302	307	313	317
$V_{G3T} \pm 1$	818	834	850	866	882	898	920	930
$V_{G3B} \pm 1$	570	581	592	603	614	625	639	647
$\Delta V_3 \pm 1$	245	250	255	260	268	273	281	283

Table 2.2: Voltage measured on each GEM preamplifier using HV-voltage divider circuit.

The high voltage divider circuit included a high-pass filter that provided a trigger (trigout) signal when the electrons left the last GEM preamplifier. One of the techniques used to improve the detector signal was to use a high-pass filter that was in contact with the bottom side of the third GEM preamplifier. When the electron stream left the last

GEM preamplifier moving toward the charge collector, a positive current was produced through a high-pass filter. The threshold frequency was dependent on a capacitor and resistor in the high-pass filter. For instance, connecting 100 pF capacitor with 1 MΩ resistor, connected to ground, created a high pass filter with a cut off frequency of 10 kHz. Figure 2.9-b describes the circuit of the high-pass filter used in the high voltage divider circuit.

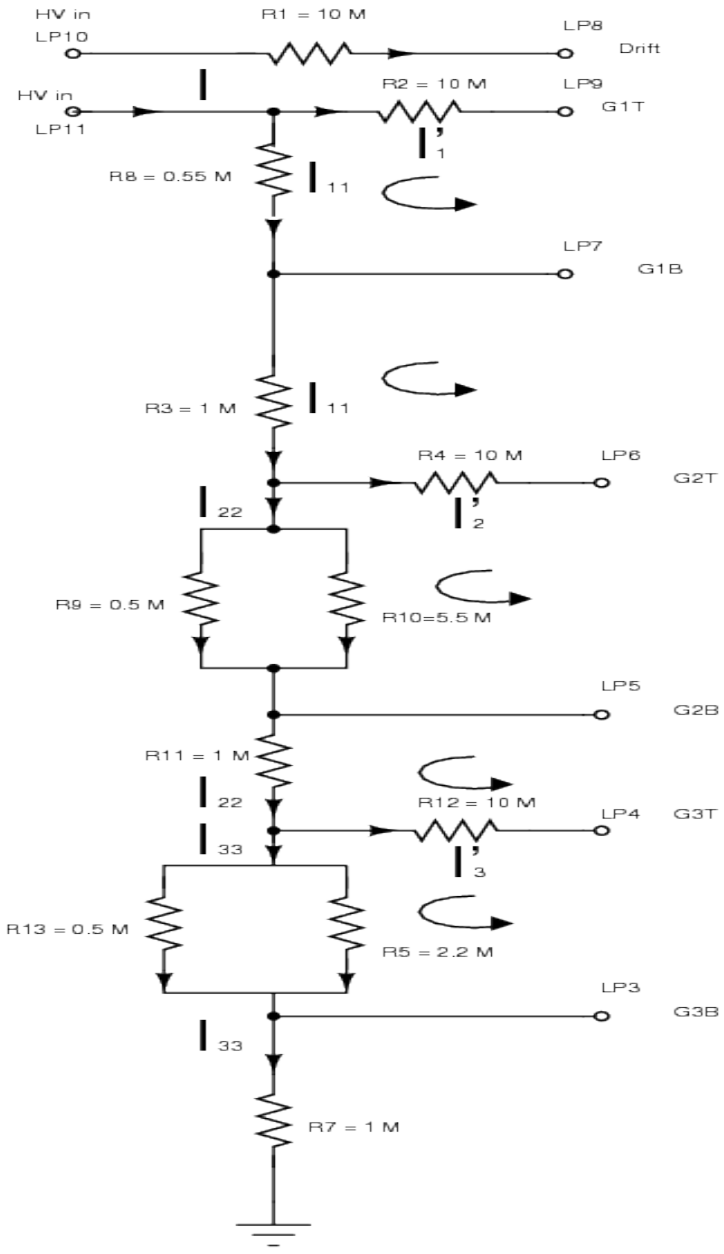

(a)

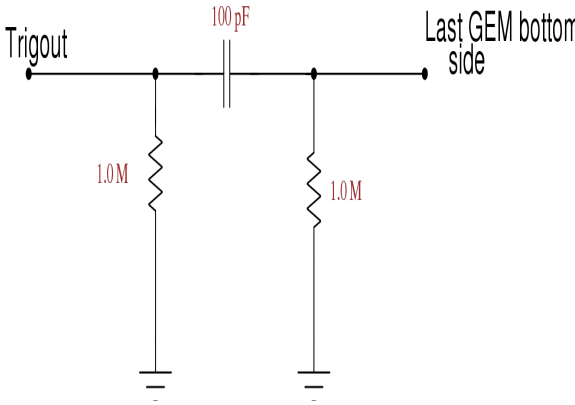

(b)

Figure 2.9: (a)The components of the HV-divider circuit. (b)High-pass filter design circuit.

2.4 Detector operation

The high voltage divider circuit provided the voltage to the GEM preamplifiers using a high voltage power supply. A four-channel digital power supply, CAEN N470, provided the voltage to the high voltage divider circuit, which distributed the appropriate voltages to the top and bottom sides of each GEM preamplifier. A signal on an oscilloscope was first observed when the provided voltage reached 2.55 kV and 3.25 kV to the GEM preamplifiers and the cathode respectively. This corresponded to a drift electric field of 700V/cm. The first and last GEM preamplifiers had a voltage difference of 304 V and 245 V respectively.

The spark discharge probability increased with increasing the applied voltage on each GEM preamplifier. To avoid the negative effect of continuous spark discharge, a protection circuit was connected to trip the high voltage power supply the instant any spark discharge occurred. However, the probability of spark discharge is very low when the detector was operated at 2.87 kV and 3.87 kV for the GEM preamplifiers and the cathode respectively.

The protection circuit from spark discharge effect is sensitive to spark discharges wider than 15 μm. The power supply was connected to the spark discharge protection circuit that had the detector signal connected to a Lemo 00 input to activate a kill option for the power supply. While operating the detector, the kill Lemo 00 input was connected to the detector charge collector so that if a spark discharge happened and its signal was wider than 15 μs, the kill option tripped all the channels of the power supply.

2.5 Data Acquisition (DAQ) System

A DAQ (data acquisition) system was used to measure the detector output using a charge to digital converter (QDC) as a part of an electronic circuit to save the charge spectrum on a data file in a storage hard drive connected to the CPU. An electronic circuit consisting of a number of NIM bin modules was used to measure the charge by a CAEN V792 QADC module (VME module)as shown in Figure 2.10. The QDC module required an integrating gate 1 μs wide to measure the analog pulse that comes from the detector's trigger output. The QADC measures up to 400 nC as reported from the manufacturer that were sampled to 4096 channels to provide each channel with storage capacity of 100 fC.[27] A trigger supervisor communicated with the QDC module using a square pulse that was delayed to 6 μs in time relative to the QDC gate.

Furthermore, the VME crate was connected to a CPU unit that had the CODA 2.6.1 software package which was responsible for collecting the data through the VME crate and saving the measurements in a data file on an event by event basis. A script was used to convert the collected data file to an n-tuple ROOT file to analyze the data using a ROOT software package.

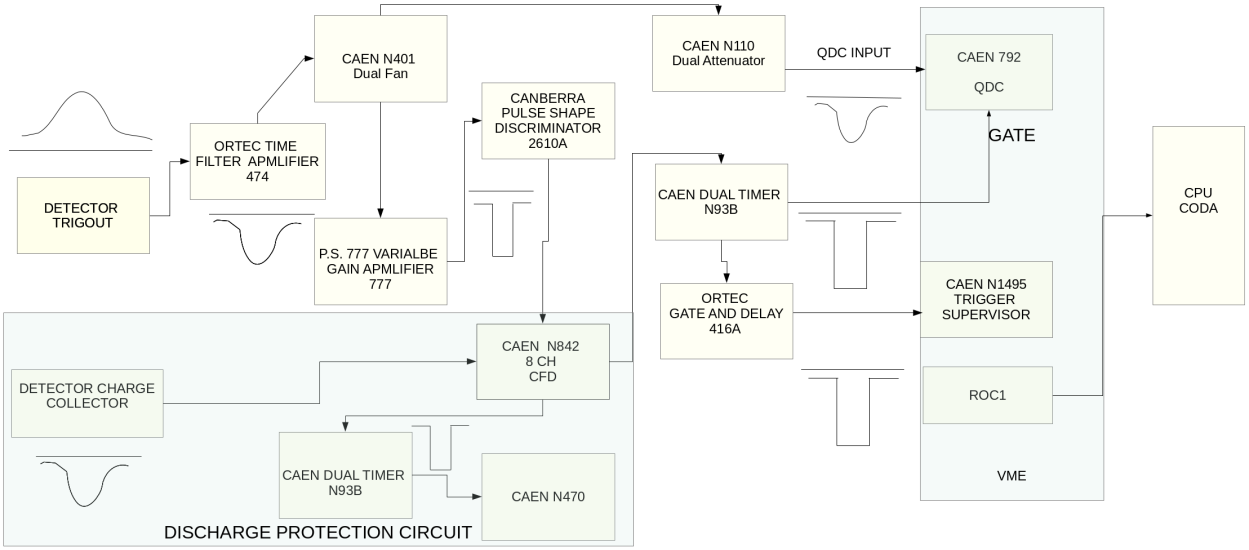

Figure 2.10: Flow chart for the signal processing circuit and the spark spark discharge protection circuit.

Chapter 3

Simulation

The main purpose of performing the Monte Carlo simulations was to estimate the number of free electrons that reached the readout plate. U-233 emitted three types of particles: α, β, γ-particles. Each particle has specific interactions with surrounding medium that can be simulated when information about an incident particle can be provided such as the kinetic energy and the emission rate.

Estimating the number of free electrons provided information about the collected charge that contributed in the QDC charge spectrum. The collected charge by the QDC on a specific channel number did not have any indicator for its source (ionizing particle). However, simulating the ionizing particles in the same conditions that surrounded the collected charge spectrum gave an indication to the amount of charge collected by the readout for each ionizing particle within a calculated statistical error. In all the particle simulations, ionization was the dominant interaction between the incident particles and the atoms and molecules of the surrounding gas.

This chapter discusses the simulations of ionization for all the ionizing particles in the drift region that were expected to share in the collected charge by the charge to digital converter (QDC). Additionally, it discusses the effect of the fiber glass shutter on the initial charge deposited in the drift region by each particle when the shutter was open and when it was closed. It discusses the electron multiplication of the triple GEM preamplifier detector depending on its voltage settings.

3.1 α-Particle Ionization

Simulations of using GEANT4[7] and Srim & Trim[8] benchmarked published data for α-particles ionization in Ar/CO_2 gas. The ENDF-database specified the emission rates and the energies for each α-particle that the U-233 coating emitted in the drift region. Then, GEANT4 and Srim & Trim estimated the deposited energy of an α-particle emitted from the U-233 coating, evaluated the number of primary and secondary electrons that were produced in the drift region, and finally showed the impact of the fiber glass shutter on the deposited charge and the detected rates of the α-particles.

3.1.1 α-Particle Emission Rates

α-particles have specific relative emission rates when they are emitted from U-233 radioactive nuclei. Figure 3.1 shows the rates of the α-particles emitted from the radioactive nuclei in a U-233 coating which is contaminated with Th-232.[28] For example, U-233 emits 85% of its α-particles with an energy of 4.85 MeV while Th-232 emits 80% of its α-particles with an energy of 4.00 MeV.

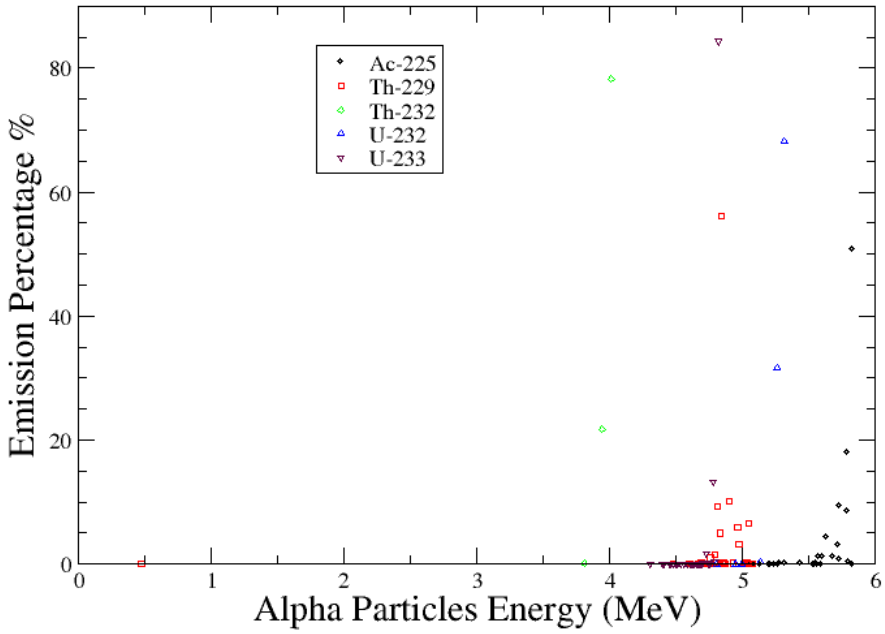

Figure 3.1: The mission rates of α-particles from nuclei in U-233 coating.

Furthermore, Figure 3.1 shows the α-emission rates of nuclei that are expected to emit α-particles after exposure to a neutron flux.[2] If using this as a neutron detector, it should be aware that a neutron flux produces new α-emitters, such as U-232, which emits 70% of its α-particles with an energy of 5.3 MeV. However, the effect of U-232 is

considered negligible due to its low concentration compared to the other α-emitters. It is important to note that all the emission rates in Figure 3.1 are relative emission rates for all the emitted α-particles from the same radioactive nucleus.

3.1.2 Primary and Secondary Ionization of α-Particles

α-particles produced primary electrons which produced secondary electrons as they passed through the drift region of the detector. α-particles' transport through the drift region ionized the gas which produced primary electrons. These primary electrons scattered and ionized the gas again to produce secondary electrons. Simultaneously with ionization, the drift electric field decreased the probability of free electron reattachment to the ions and collected the free electrons to transport them toward the first GEM preamplifier.

The drift electric field affected the number of the electrons collected in pure argon gas. When an α-particle traveled in pure argon, it liberated up to 3×10^4 electrons through primary and secondary ionization without any electric field.[29] Saito et al. measured the number of primary and secondary electrons in region of 4.7 kV/cm drift electric field for 5.49 MeV α-particles. Saito's group collected 2×10^5 electrons from the drift region using a charge collector, and their measurements showed that the collector counted almost all the electrons from ionization in the drift region.[30] This demonstrated that adding an electric field decreased the probability of any electron-ion reattachment.

The model used in simulating the number of primary and secondary electrons in GEANT4 and Srim & Trim was tested by estimating the α-particles range in Ar and CO_2 gases separately. As shown in Figure 3.2-a and Figure 3.2-b, both packages simulated the range of α-particles in Ar and CO_2 gases with similar gas conditions of a pressure of 1 atm, a temperature of 293 K, and a density of 1.64 mg/cm^3. GEANT4 accurately simulated the α-particle range in Ar and CO_2 gases, matching Hanke and Bichsel measurements.[31] However, the Srim & Trim model estimated the range 50% less than the range measured by Hanke and Bichsel in pure argon[31] and estimated the same range of 4 cm for the energies of all the alphas in CO_2 gas.

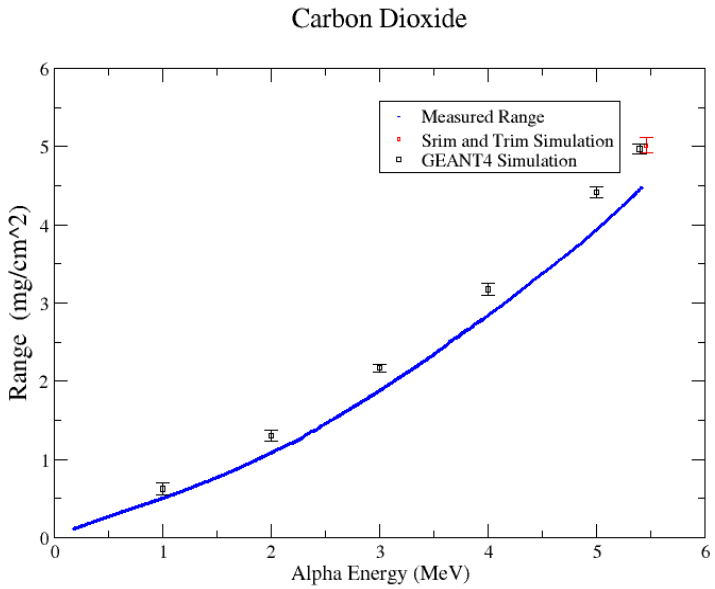

(a)

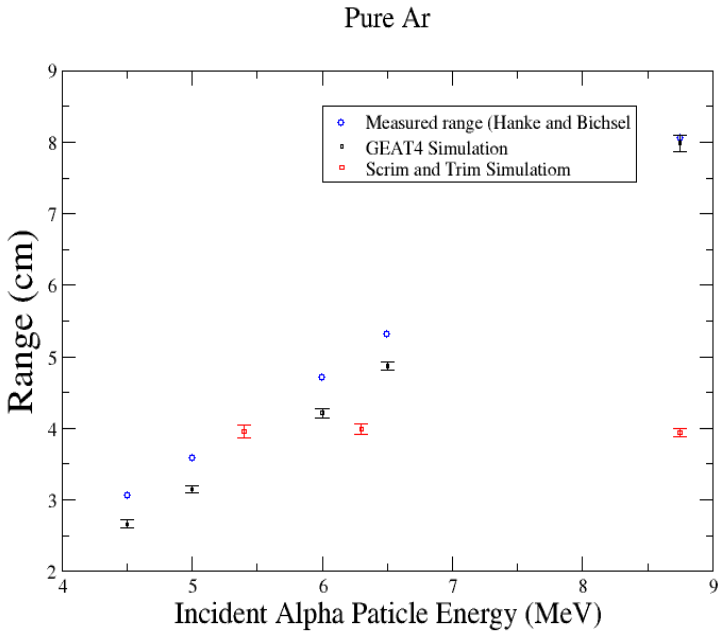

(b)

Figure 3.2: Range of α-particles in(a)CO_2 gas. (b) Ar-gas.

Consequently, GEANT4 was used to simulate the number of primary and secondary electrons in 1 cm of 90% Ar-gas and 10% CO_2 gas mixture as shown in Figure 3.3-a and Figure 3.3-b. GEANT4 estimated 2.1×10^5 secondary electrons when a 5.49 MeV α-particle penetrated 1 cm of the same gas mixture without any electric field. This was close to Saito's measurements of 2×10^5 electrons.[30] It could be interpreted that the energy and range cuts used in the GEANT4 simulation were set to count for electrons of a specific range, and the reattachment of free electrons was for all the electrons that had lower ranges than the one specified in the range cut.

On the other hand, α-ionization simulation performed by Srim & Trim in a pure Ar gas agreed with the data reported by Sauli.[29] Srim & Trim estimated 1 MeV energy deposited by the incident α-particles in pure Ar-gas which made the final number of free electrons be 3.75×10^4 electrons. If the minimum energy for producing an ion-electron pair in the same gas is w = 26.7 eV/ip, then the simulations agreed with the number of free electrons reported by Sauli for α-particles passing the pure Ar-gas without any electric field.[29]

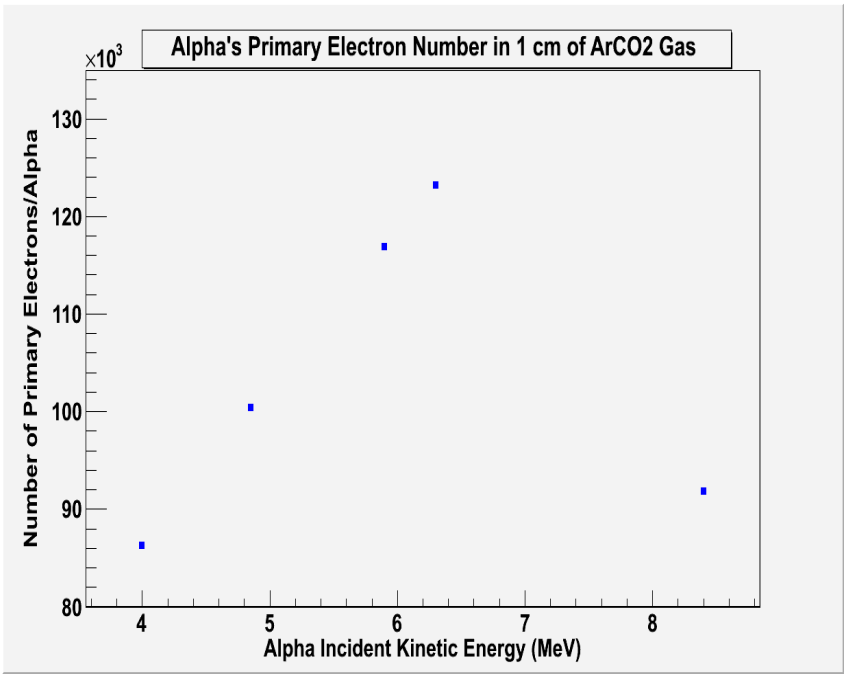

(a)

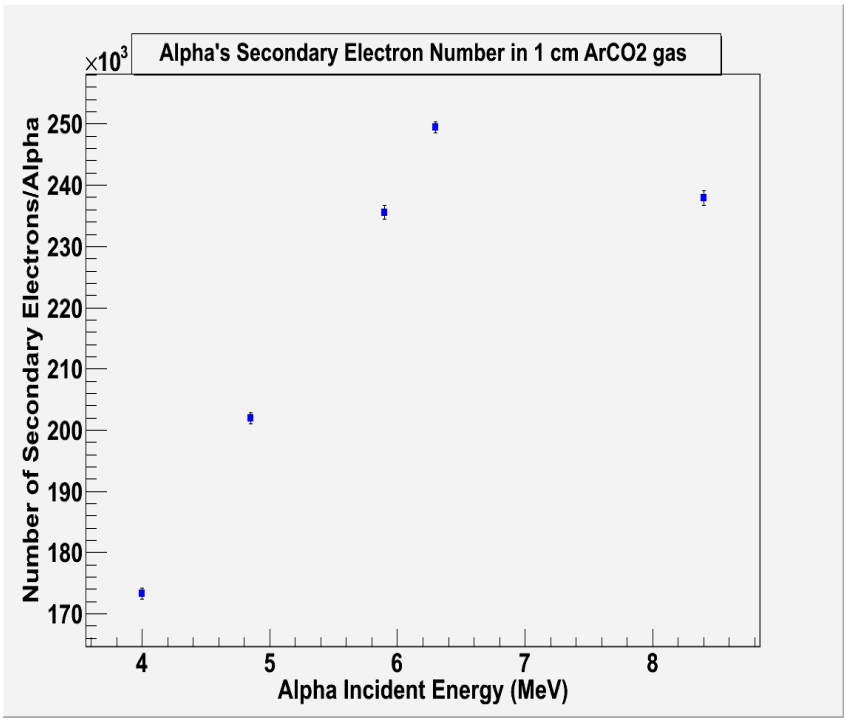

(b)

Figure 3.3: (a)Number of primary electrons (b)Number of secondary electrons of the emitted α-particles in 1 cm of 90% Ar-gas and 10% CO_2 gas mixture

3.1.3 Escaping α-Particles and Self-Absorption of U-233 Coating

The radioactive coating thickness has an effect on the rate and kinetic energy of the emitted α-particles, which is known as coating self-absorption.[32] A 30 μm thick U-233 coating decreased both the emission rate and kinetic energy of an α-particle that escaped from the U-233 coating. The amount of the deposited energy was dependent on the range of the α-particles in the U-233 coating which determined the energy of the escape α-particles before passing the drift region.

GEANT4 simulated the self-absorption of an α-particle when it passed through the U-233 coating and the drift region. The energy of the escaped α-particles from the U-233 coating, number of secondary electrons, and the range of the α-particle transmission through the drift region were all simulated using GEANT4. The simulation model used a 30 μm thick U-233 coating with a density of 10.97 g/cm^3 to determine the relationship between the coating depth and the percentage of penetration for an α-particle of an initial energy of 4.85 MeV. Figure 3.4-a the energy of escaped α-particles and percentage of penetration as a function of depth, and Figure 3.4-b shows the energy of the escaped α-particles and the number of their secondary electrons produced in the drift regions.

GEANT4 simulation showed that the maximum depth of the α-particles of energy of 4.85 MeV that were able to ionize the gas in the drift region was 5 μm passing the drift region with an energy of 0.82$\pm$0.1 MeV. When the coating depth was 5.5 μm, the energy of α-particles was only 0.31$\pm$0.05 MeV, and only half of the escaped ones that energy produced 7000 secondary electrons. At 5.5 μm depth, some of the emitted α-particles reached the drift region without ionizing the gas and were counted with the others that ionized the gas in that region. At depth greater than 5.5 μm, all the α-particles were completely absorbed by the U-233 coating.

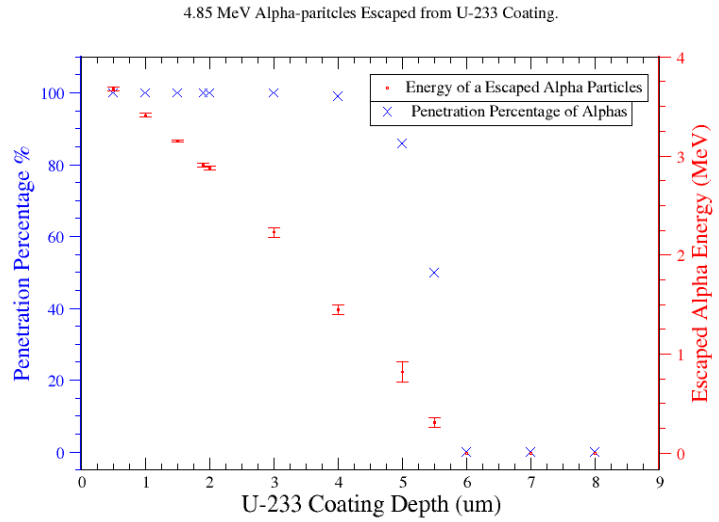

(a)

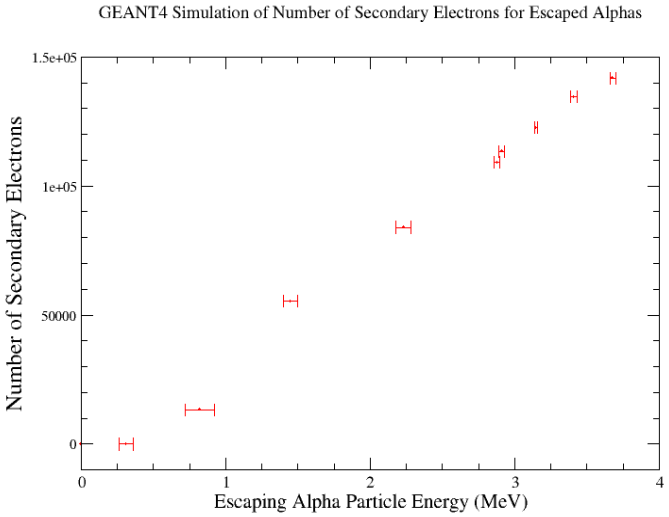

(b)

Figure 3.4: (a)Escaped α-particles from U-233 coating depth vs. penetration percentage and its escaping kinetic energy.(b)Number of secondary electrons for the escaped α-particles.

3.1.4 α-Particle Transmission Through the Fiber glass Shutter

The GEANT4 simulation tested the ability of an fiber glass shutter to stop α-particles that were emitted from the U-233 coating. GEANT4 predicted the α-particle energy that could completely penetrate the fiber glass shutter. An α-particle had to have a minimum energy of 55 MeV for a complete transmission through the 1 mm fiber glass shutter as shown in Figure 3.5.

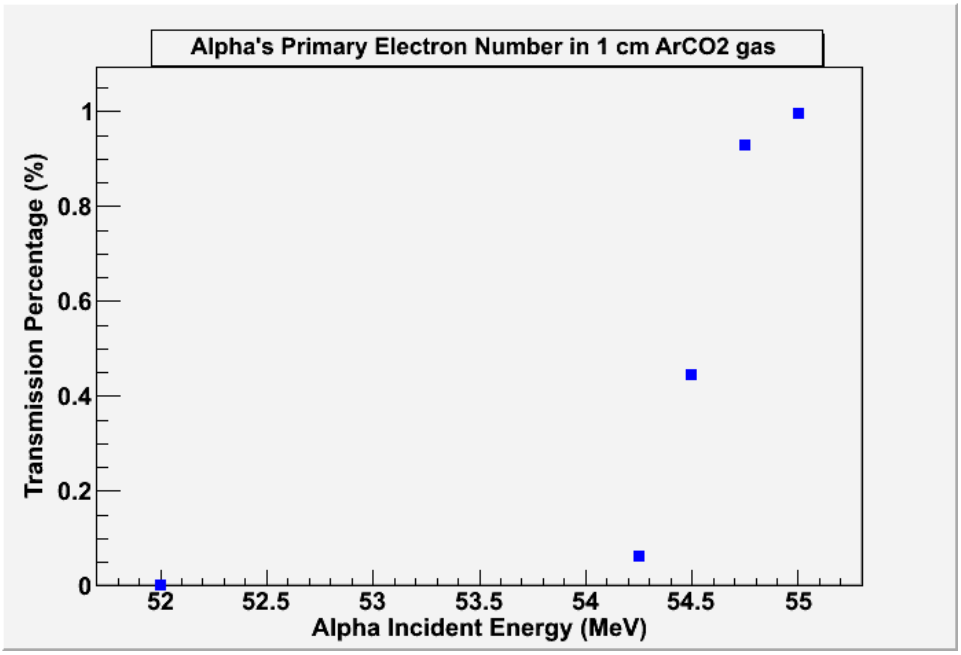

Figure 3.5: α-particles transmission percentage through 1mm fiber glass shutter.

As discussed in Section 3.1.1, the emitted α-particles from the U-233 coating had a maximum energy of 8.40 MeV with an average energy of 4.00 MeV and 4.85 MeV for Th-232 and U-233 respectively. In Section 3.2.2, it will be shown that the shutter was able to stop all the emitted α-particles and their primary electrons produced in the 1.5 mm distance between the shutter and the source.

3.2 Ionization by β^--Particles, Internal Conversion and Auger Electrons

GEANT4[7] and Garfield[16] were used for simulating electron ionization in 90% Ar and 10% gas mixture. GEANT4 performed the simulation of the electron ionization in the drift region to estimate the number of primary electrons, then to estimate the number of secondary electrons for all the emitted electrons from U-233 radioactive coating. The U-233 coating is contaminated with Th-232 and other radioactive elements that appear after exposing the detector to a neutron flux. Furthermore, GEANT4 was used to simulate the effect of the fiber glass shutter on the electron ionization when the shutter was closed. Finally, Garfield was used for simulating the electron multiplication by the GEM preamplifiers, and it also simulated the electron ionization in the drift region.

3.2.1 Electron Emission Rates

U-233 coating emits electrons in different rates from different radioactive nuclei, and part of these nuclei appear after a neutron capture by Th-232. U-233 coating emits electrons at different rates and energies as reported by ENDF-database.[2] Figure 3.6 shows all the electron emission rates of more than 9% in the red box, which were the most probable electron energies that would make an ionization in the drift region and might influence the detector signal.

Additionally, Figure 3.6 shows the electron emission rate is greater than 20% for two different energies before a neutron capture occurs by Th-232.[33] After the Th-232 neutron capture, β-particles and Auger electrons emission rates increase as result of daughter radioactive nuclei such as Th-233 and Pa-233 as shown in Equation 3.1, or the gamma emission rates increase by U-232[33] as shown in Equation 3.2. Pa-233 and Th-233 emit 5-30% and 20% of Auger electrons with an energy between 100-400 keV and 200 keV respectively. In addition, Pa-233 and U-233 emit β-particles that reached up to 560 keV

Radioactive Nucleus	Half life
U-233	1.59×10^5 years
U-232	68.90 years
Th-233	22.3 minutes
Th-232	$1.41\ \times10^{10}$ years
Pa-233	26.97 days

Table 3.1: Half lives of the radio-nuclei that emit Auger electrons and β-particles emitters.

and 1.2 MeV respectively, which would influence the detector signal.[2] The half lives of all the electron emitters are shown in Table 3.1.

$$Th_{90}^{232} \xrightarrow{n} Th_{90}^{233} \xrightarrow{\beta^-} Pa_{91}^{233} \xrightarrow{\beta^-} U_{92}^{233} \tag{3.1}$$

$$Th_{90}^{233} \xrightarrow{\beta^-} Pa_{91}^{233} + n_0^1 \rightarrow Pa_{91}^{232} + 2n_0^1 \xrightarrow{\beta^-} U_{92}^{232} \tag{3.2}$$

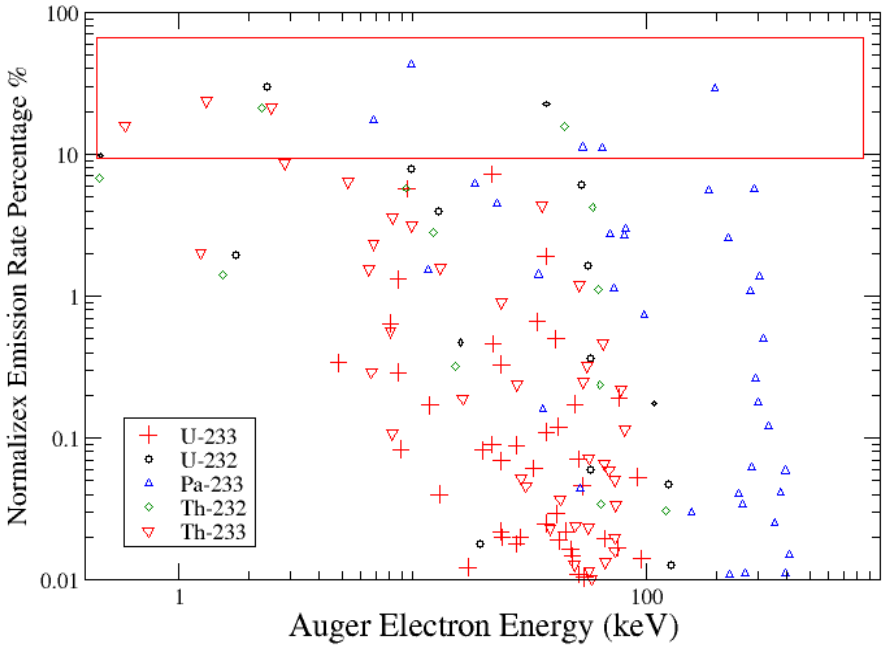

(a)

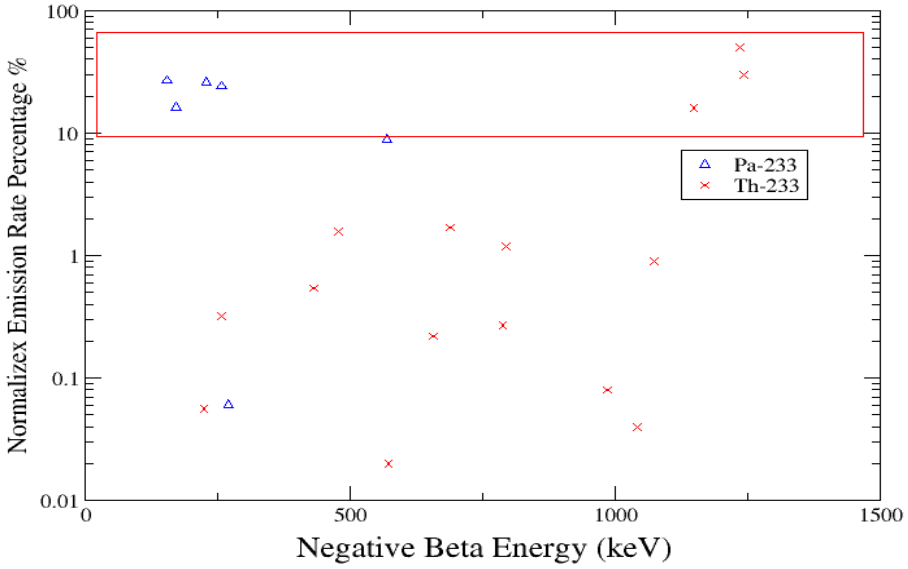

(b)

Figure 3.6: U-233 coating emission rates of (a)Auger electrons. (b)β^--particles.

3.2.2 Electron Primary and Secondary Ionization

The electron ionization simulation was performed by the Garfield[16] simulation package in the drift region inside the detector. The Garfield simulated the ionization by electrons in the drift region that contained a mixture of 90% Ar-gas and 10%CO_2 gas by volume. It estimated the number of free electrons liberated by ionization depending on the incident electron energy as shown in Figure 3.7. The number of free electrons which was 50-80$\pm$15 free electrons, was almost constant for all the electrons in the selected gas.

Similarly, GEANT4[7] and ESTAR[34] estimated the number of free electrons for the incident electrons in the same energy range which ionized the drift region. GEANT4 simulated the number of primary and secondary electrons that are liberated in the drift region, and the number of free electrons increased by increasing the kinetic energy of the incident electrons until it reached 100 keV. At higher energies, the incident electrons produced the same number of free electrons, about 200, in the drift region. ESTAR calculations showed that the number of free electrons decreased when the energy of the incident electrons increased. However, 150 free electrons were repeatedly estimated when the incident electron energy was greater than 100 keV.

Although all the models agreed that the number of the secondary electrons did not change when the electron energy was greater than 100 keV, they showed different estimations for the number of liberated electrons. ESTAR overestimated the number of free electrons when the incident electron energy was smaller than 100 keV. Ionization was not the dominant process. There were other physical processes that simultaneously occurred, such as electron scattering, electron excitation, partial ionization (for CO_2)gas, and atomic vibrations. The cross sections of the previous physical processes were incorporated in Garfield and GEANT4 along with the cross section for electron ionization. Both packages agreed to within two standard deviations.

ESTAR estimated the number of free electrons depending only on Bethe-Bloch equation which calculated the energy loss in the drift region by the emitted electrons from U-233 coating. Then, the number of liberated electrons in the drift region was estimated

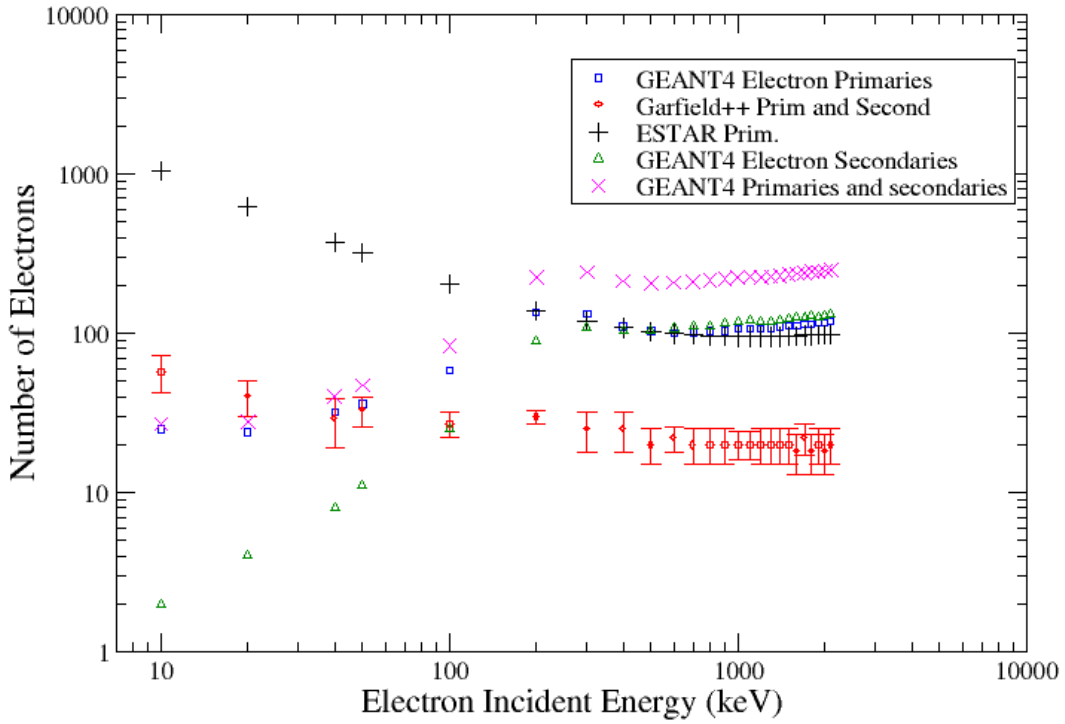

Figure 3.7: Number of free electrons for the emitted electrons from U-233 coating in 90% Ar-gas and 10% CO_2 gas mixture estimated by different software packages.

by dividing the energy loss by 26 eV which is the minimum energy necessary to produce an ion-electron pair in 90% Ar and 10% CO_2 gas mixture as shown in Figure 3.7.[34] However, both GENAT4 and Garfield estimated the number of free electrons in the drift region considering both of the electron ionization cross section and electron scattering cross sections along with calculations to complete the simulations.

Both Garfield and GEANT4 agreed that 55±10 electrons was the average number of free electrons produced by the incident electrons in the drift region within two standard

deviations when their incident energies were below 100 keV. However, Garfield showed the number of free electrons in average was the same as the energy of the incident electrons increased to more than 1 MeV, and GEANT4 estimated larger number of primary electrons that reached 200 electrons and 300 electrons for primary and secondary electrons as shown in Figure 3.7.

ESTAR agreed with the number of primary electrons estimated by GEANT4. ESTAR indicated that the electron deposited energy in the gas was all used in liberating electrons. GEANT4 estimation for primary electrons agreed with ESTAR when the energies of the incident electrons were larger than 100 keV which was 150 electrons. The total number of free electrons (primary and secondary electrons) simulated by GEANT4 was 300 electrons which showed that GEANT4 simulated the primary electrons whose energy were larger than 100 keV to simulate the number of secondary electrons.

Both GEANT4 and Garfield considered the cross section of electron ionization and electron scattering in the selected gas to estimate the number of primary electrons. GEANT4 uses Moller and Bhabha scattering for calculating the scattering cross section for electrons of energy with a kinetic energy cut of 1 keV. The delta rays are sampled and their direction along with the incident electrons are calculated depending on the conservation of momentum.[35] On the other hand, Garfield uses Magboltz software package[15] to calculate (stored) the electron-atom (electron-molecule) ionization and scattering cross sections to calculate the electron avalanche or electron drift velocity in the electric field region using the class AvalancheMicroscopic.[36]

As a result, number of simulated free electrons by incident electrons in specific energy range were comparable within accepted uncertainty limits. Each simulation package indicated that electrons of energy more than 100 keV deposited different amount of energy in gas, nevertheless, they all agreed that the estimated deposited energy remained constant. When the electron incident energy was less 100 keV, the results varied depending on each package cross section calculations (or stored) for the electron interactions with the gas composites.

3.2.3 Electron Transmission through an fiber glass Shutter

The fiber glass shutter completely stopped the emitted electrons from U-233 coating with energy smaller than 500 keV. Figure 3.8 shows the predicted transmission of electrons that passed through a 1 mm fiber glass shutter when the U-233 coating was completely covered by the fiber glass shutter. The shutter stopped all Auger electrons from U-232, Pa-233, and Th-232 since their energies are less than 500 keV as shown in Figure 3.6-a.

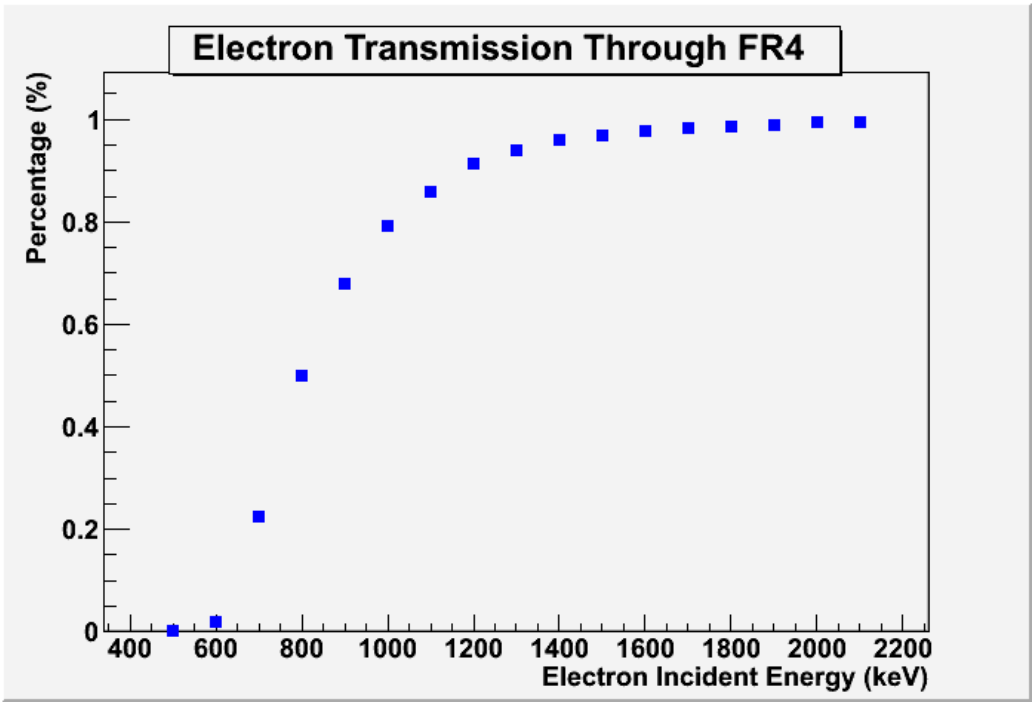

Figure 3.8: Transmission percentage of the emitted electrons through a 1mm fiber glass shutter.

On the other hand, β-particles with an energy greater than 500 keV penetrated the fiber glass shutter during the exposure to the neutron flux. The energy of Pa-233 β-particles reached 570 keV at 9% emission rate, and their transmission probability was 0.02. Similarly, the emitted β-particles from Th-233 had energies between 1000 keV and 1200 keV with emission rates reached 30%, which made their transmission probability

80-90% through the fiber glass shutter as shown in Figure 3.8.

Therefore, β-particles of energy more than 700 keV might have contributed to the deposited charge in the drift region regardless of the position of the fiber glass shutter. However, due to the dependence of their emission rate on the percentage of Th-232 interacting with the incident neutrons, the expected β-particles that passed the drift region could not be estimated unless more information provided about the neutron flux.

3.3 Triple-GEM Preamplifier Gain

Garfield[16]simulated the electron multiplication in Ar/CO_2 gas for the triple GEM detector. Garfield uses HEED[37] and Magboltz[15] software packages to simulate the ionized electrons and their drift velocity distribution. Magboltz uses the longitudinal and transverse diffusion coefficients along with the drift velocity in Ar/CO_2 gas to solve Boltzmann's equation[14] in 3D. HEED simulates the ionization by electrons in the gas in order to simulate the electron multiplication of the triple GEM detector. Garfield also uses a finite element method (FEM) software package ANSYS[38] to map the electric field in the holes of the GEM preamplifiers for three successive layers, and in the regions around them according to the voltage on each GEM preamplifer and on the detector cathode.

At the beginning, Garfield simulated the electron multiplication in the drift region inside the detector. When an electric field of 700 V/cm transported electrons through the 1 cm of the drift region, the electrons interacted with the gas atoms and molecules. According to the Garfield simulation for the ionizatoin in the drift region, electrons liberated 8±1 electrons before they reached the first GEM preamplifier. Ionization results compared to GEANT4[7] simulations when the electron energy reached to 1100 keV were previously shown in Section 3.2.2 along with the results from ESTAR calculations.[34]

Published data for the gain of a triple GEM detector in a 93% Ar-gas and 7% CO_2 gas mixture were benchmarked by using Garfield simulation code[16] before simulating the triple GEM gain in 90% Ar-gas and 10% CO_2 gas mixture.[39] Figure 3.9-a shows that Garfield estimated almost the same measured gain for the triple GEM preamplifier detector when the voltage difference for each GEM preamplifier was 300V and 320V. However, when the voltage exceeded 340V, the simulation model overestimated the gain 25% more than the measured value.

Consequently, the Garfield code was used to simulate the multiplication of the triple GEM detector when the source voltage was 2.87 kV and the cathode was 3.57 kV in 90 % Ar-gas and 10% CO_2 gas mixture. At this voltage, the voltages of the GEM preamplifiers

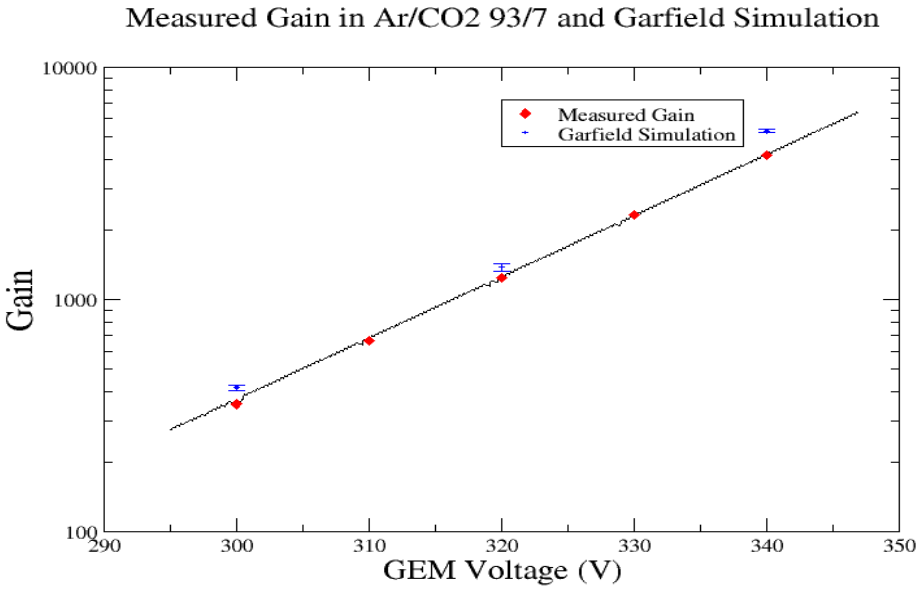

(a)

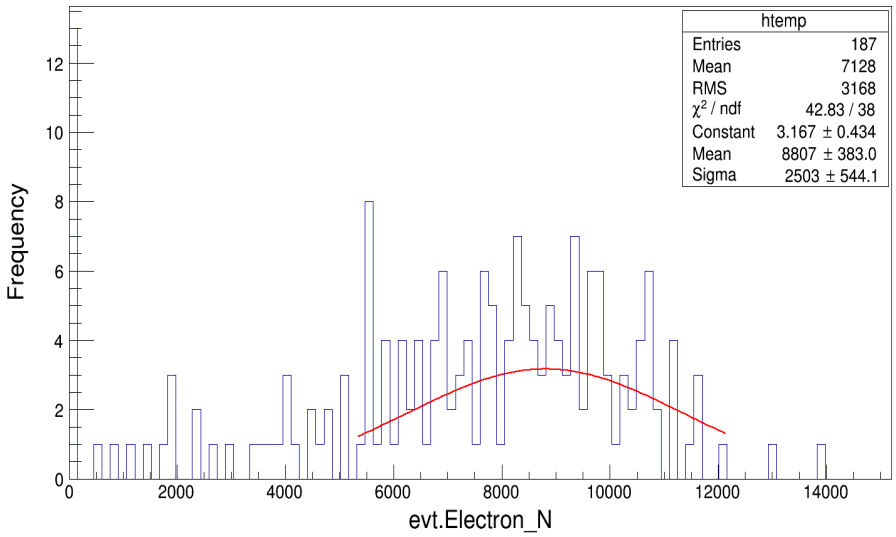

(b)

Figure 3.9: (a)Garfield simulation of the predicted gain with the measured gain for Ar-gas 93% and 7% CO_2 gas mixture. (b)Triple preamplifiers gain with 700 V drift voltage, ΔGEM_1 =338 V, ΔGEM_2 =313 V, and ΔGEM_3 =281 V, and an ionization potetial of 200 eV.

gradually dropped from 338 V for the first GEM preamplifier to 281 V for the last one as shown previously in Table 2.2. Figure 3.9-b shows that the Garfield simulation was about $(6.1 \pm 164) \times 10^3$ electrons for the electron multiplication with a drift electric field of 700V/cm at room temperature and a pressure of 1 atm.

3.4 γ-Particle Ionization

GEANT4 also simulated γ-radiation, the last type of radiation emitted by U-233 that can cause an ionization in the drift region. GEANT4 simulated the ionization of γ-particles emitted from U-233 coating when it interacted with Ar/CO_2 gas. According to the energy range of the incident γ-particles, photo-absorption and incoherent scattering were considered as common interactions. More details about simulating the ionization of γ-particles will be illustrated in the next sections.

3.4.1 γ-Particle Emission and Ionization

The emission rates of γ-particles were reported by ENDF-database for each radioactive nucleus in the U-233 coating.[2] Installing the U-233 coating on the cathode exposed the drift region to γ-particles from different radioactive nuclei, such as U-233 and Th-232. If the U-233 coating was exposed to neutrons, new nuclei such as U-232, Pa-233, and fission fragments might be produced. These nuclei emit γ-particles that could also ionize the gas. Table 4.1 The possible sources of photons that are emitted from U-233 coating including the nuclei produced during the exposure to neutron flux.[2]

Radioactive nucleus	γ-particle average energy (keV)	X-ray average energy (keV)
U-233	0.222 ± 0.003	0.888 ± 0.107
Th-232	0.197 ± 0.011	1.175 ± 0.094
U-232	0.222 ± 0.1	1.903 ± 0.138
Pa-233	176.507 ± 1.284	41.057 ± 0.563
Th-233	34.15±0.17	2.83±0.13

Table 3.2: Average energy of γ-particles and X-rays reported by ENDF-database.

Most of the γ-particles emitted from the radioactive nuclei interacted by photo-absorption in the drift region. The exception was the higher energy ones from Pa-233.

Photo-absorption occurs when a photon gives almost all of its energy to an electron around the nucleus. The process is dependent on the cross section as a function of electron energy as shown in Figure 3.10.[5] Additionally, within the same energy range, GEANT4 showed an incident photon interacted with the surrounding gas by photo-absorption, and only one electron was liberated with an energy slightly below the incident photon energy. The liberated electrons interacted with the gas again to produce primary and secondary electrons as previously illustrated in Section 3.2.2.

During the exposure to neutron beam, it will increase the ionization rate of γ-particles in the drift region. γ-particles ionization rate will be increased after induced fission events with the U-233 coating, and the emitted fission fragments mostly emit photons during their passage through the drift region.[40] In addition, the neutron flux will be mixed with photons that might ionize the gas in the drift region.

3.4.2 γ-Particle Transmission through the fiber glass Shutter

The fiber glass shutter had the ability to block γ-particles when their energy was less than or equal to 7 keV. The fiber glass shutter mostly blocked γ-particles that were emitted from U-233 coating, except for the ones emitted from Pa-233. However, low energy photons with an energy of 5 keV were attenuated and absorbed within 1.5 mm distance between the U-233 source and the fiber glass shutter. Therefore, the fiber glass shutter blocked the free electrons from the low energy ionizing photons as shown previously in Section 3.2.3. Additionally, the high energy photons from Pa-233 and Th-233 completely penetrated the fiber glass shutter and the drift region, though their emission rate was mostly negligible

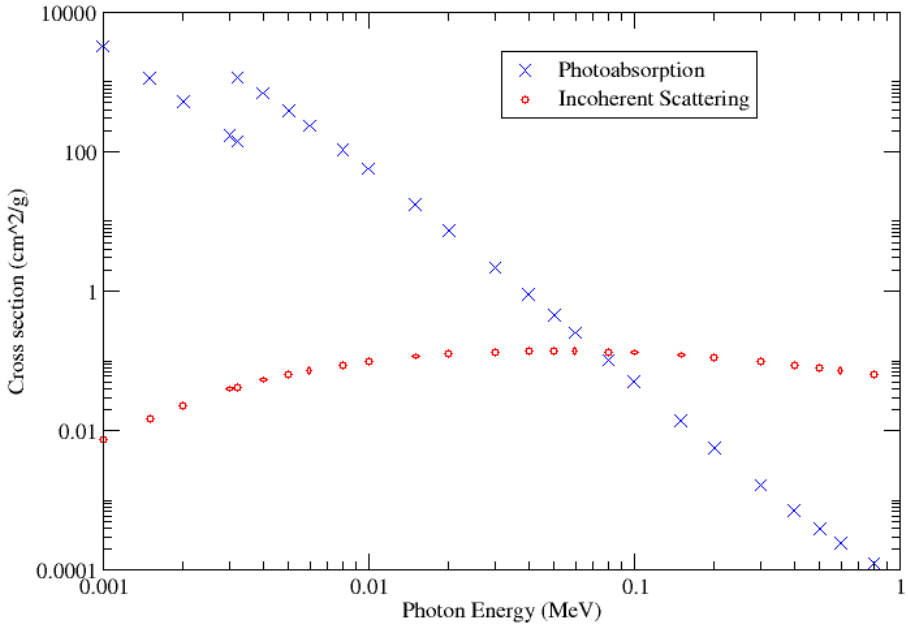

Figure 3.10: Photo-absorption and incoherent scattering cross sections for the expected energies of incident γ-particles in Ar-gas 90% and 10% CO_2 gas mixture.

since it was dependent on Th-232 concentration in U-233 coating.

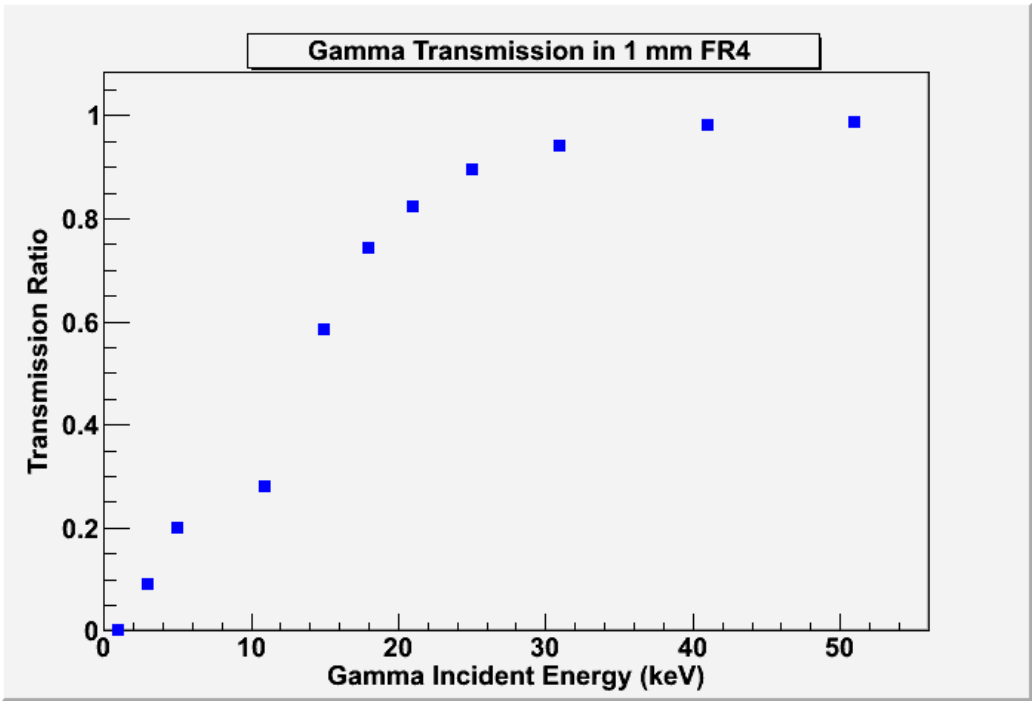

Figure 3.11: γ-particles transmission percentage through 1 mm fiber glass shutter.

Chapter 4

Experimental Setup and Measurements

The experimental measurements first characterized the U-233 coating, and the GEM detector measured the output after the U-233 coating was embedded into the detector drift region. α-particle and γ-particle spectroscopy were performed for the U-233 coating to determine the energy of emitted particles. The second part includes the GEM detector charge spectrum for U-233 coating using a VME based system that included charge to digital converter (QDC) to save it on CPU storage desk. The charge spectrum has been analyzed using ROOT[41] software package. Then the measured data were analyzed and compared to the simulation results in Chapter 3 to identify the ionizing particle as will be shown in the next sections.

4.1 U-233 Coating Characterization

4.1.1 α-Particle Spectroscopy

The α-particle spectrum was measured using a Canberra spectrometer under vacuum connected to a multi-channel analyzer. The Canberra spectrometer model 7401[42] chamber has a PIPS detector (passive implanted planar silicon) with a sesitive area of 1200 mm. The spectrometer measured the spectrum of α-particles in a low pressure environment. The pressure inside the chamber reached 16-20 μtorr. α-particles were detected after increasing the biased voltage to 20 V. The analog signal was sent to the multichannel

analyzer ORTEC model 926.[43] Figure 4.1-a shows ORTEC 926 which allowed the user to select 8120 channels to specify the energy within 0.002 MeV.

The spectrometer calibration curve was constructed using standard α-particle sources. These standard sources provided different α-particle energies that were in the range of 4.2-5.6 MeV. Figure 4.2-a shows calibration curve a linear with a slope of $(1\pm0.04)\times10^{-3}$ MeV/channel. Then the U-233 the spectrometer measured the α-particle spectrum for the U-233 coating as shown in Figure 4.2-b, which shows a main peak at 4.853 ± 0.002 MeV with a 0.1 Hz detection rate. Another peak was detected at 4.835 ± 0.002 MeV with a detection rate 0.02. The energy resolution was 4.1% in detecting the 4.853 ± 0.002 MeV α-particles.

(a)

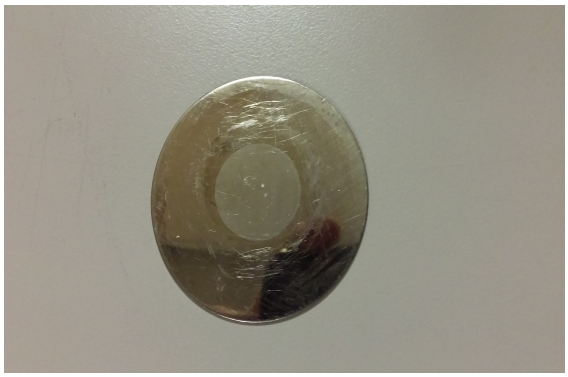

(b)

Figure 4.1: (a) Electronic modules used in α-spectruscopy. (b) U-233 coating plate.

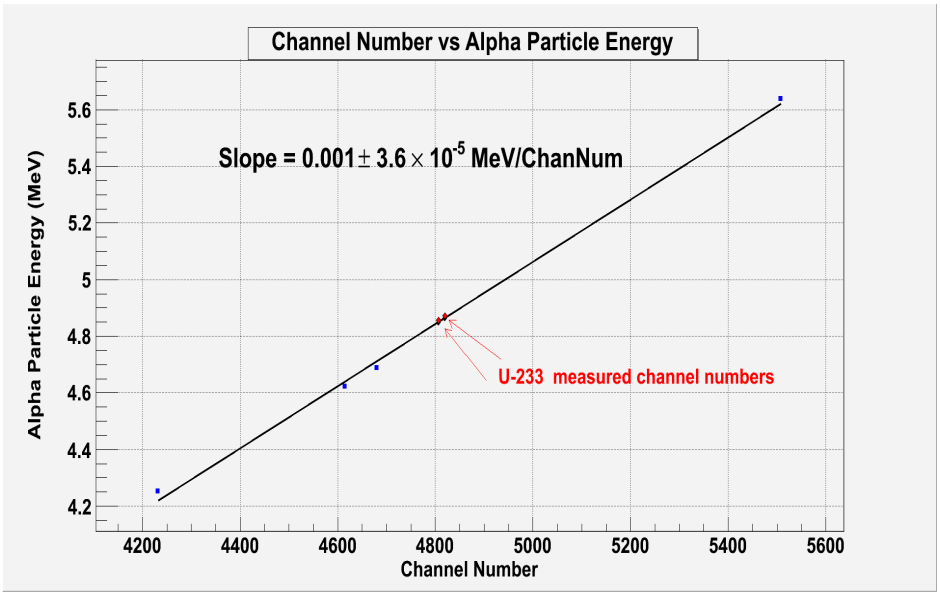

(a)

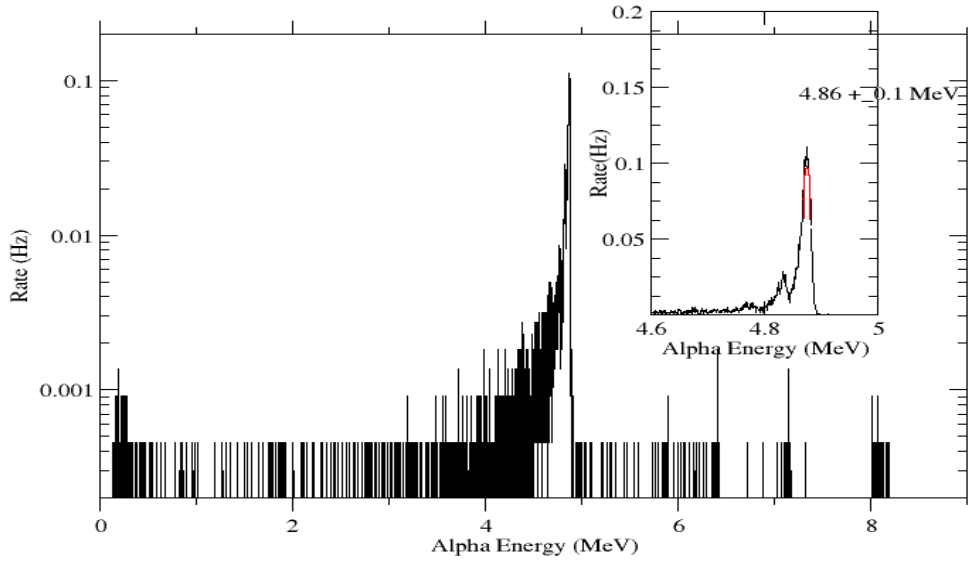

(b)

Figure 4.2: (a)α-particle spectrometer calibration curve. (b) Energy spectrum of α-particles emitted from U-233 coating.

4.1.2 γ-Particle Spectroscopy

The spectrum of γ-particles from the U-233 coating was measured using a HP-Ge detector. Figure 4.3-a and Figure 4.3-b show the HP-Ge planar detector with a Canberra amplifier model 5615 and a KD model ND579 analog to digital converter (ADC) that were used to measure the γ-particle spectrum as shown in Figure 4.3-c.[22] The detector efficiency during the detection was 3%, and the detection time was 6000s.

The measured γ-particles emitted were low in rate, but showed more than one peak measured from the U-233 coating as shown in Figure 4.4. The measured spectrum was compared to the background spectrum that had the same detection time of 6000s. Table 4.1 shows the energies of detected peaks from U-233 coating spectrum, and ENDF-database for the X-rays and γ-decay energies were used to identify the expected radio-nuclei in the U-233 coating.

(a)

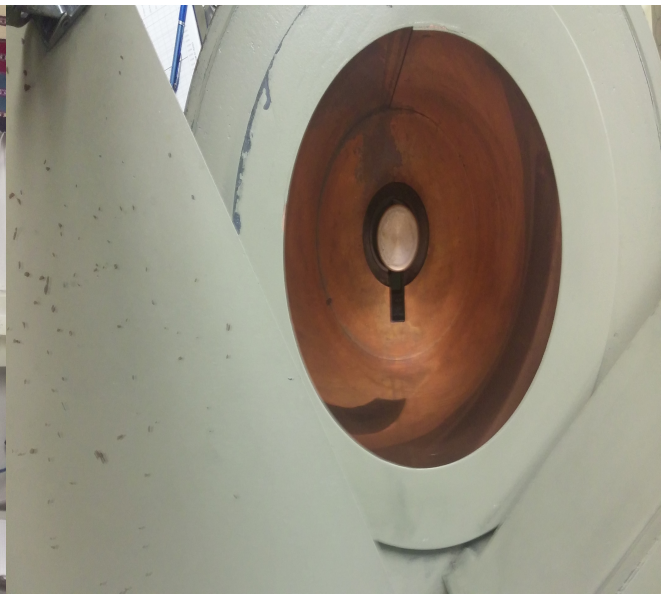

(b)

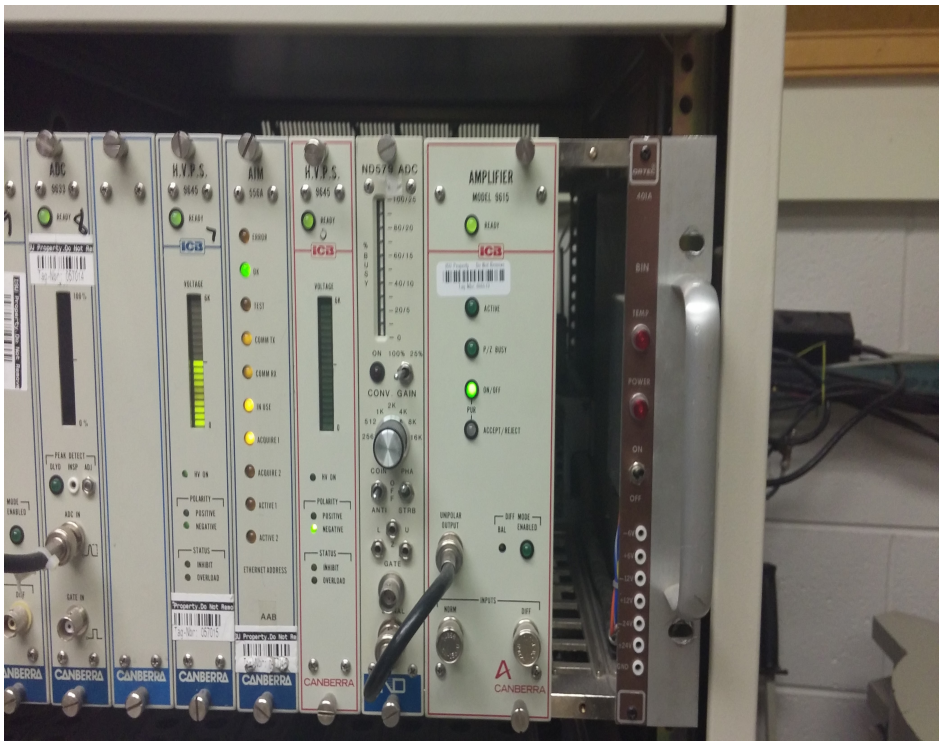

(c)

Figure 4.3: (a)HP-Ge planar detector chamber (b) and crystal with the copper shielding. (c) HP-Ge detector DAQ system.

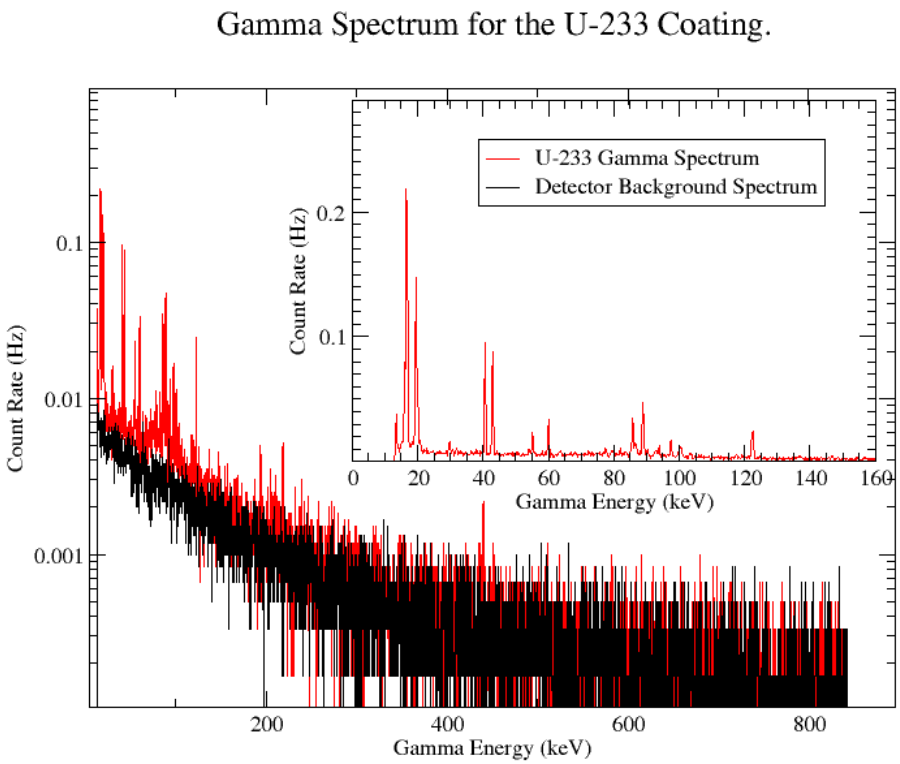

Figure 4.4: Measured γ-particles and X-rays spectrum for U-233 coating contaminated with Th-232 by HP-Ge planar detector.

The detector sensitivity to these emitted γ-particles was negligible for two reasons. First, during the detector operation, the gain of the detector was too low to amplify the ionization from these photons observe their peaks above the noise level. Second, the emitted γ-particles with the energies shown in Figure 4.4 easily penetrated the drift region without ionization even when the fiber glass shutter was closed. The probability of ionization was such that the photon mean free path was longer than the length of the drift region.

4.2 GEM Detector Charge

The differences between the detected signal from U-233 coating for open and closed shutter was observed using an oscilloscope before measuring their charge spectra. The detector output was changed when the position of the shutter was changed from an open to a closed shutter as shown in Figures 4.2-a and Figure 4.5-b respectively. The signal for open shutter had a raise time of 200±40 ns and a pulse width of 400±40 ns and the signal for a closed shutter had a raise time of 60±10 ns and a pulse width of 150±10 ns with a long tail of 120 ns.

An analog to digital charge converter CAEN V792 (QADC) was used to measure the detector's output charge collected by the charge collector. As was described in Section 2.5, the electronics setup measured the charge for different ionizing particles passing through the drift region. The data for charge measurements and their analysis using data files collected by the DAQ system and the results of the formal simulation analysis, are presented after calibrating the QDC.

Energy of the photo-peak (keV) ±1	Radioactive Nucleus	Type of Photon
17	U-233	X-rays
18	U-233	X-rays
41	U-233	γ-particle
43	U-233	γ-particle
41	U-233	γ-particle
29	Th-232	X-rays
63	Th-232	X-rays
123	Th-232	X-rays

Table 4.1: U-233 coating photo-energies measured by HP-Ge planar detector.[2]

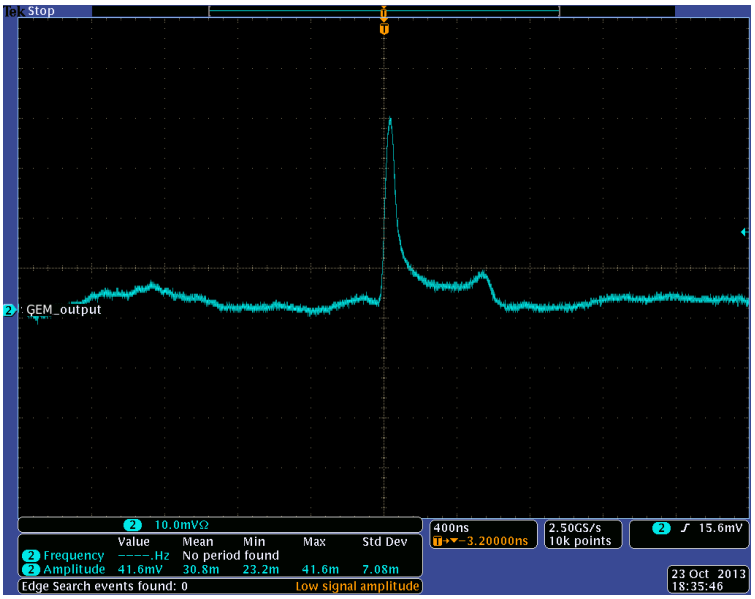

(a)

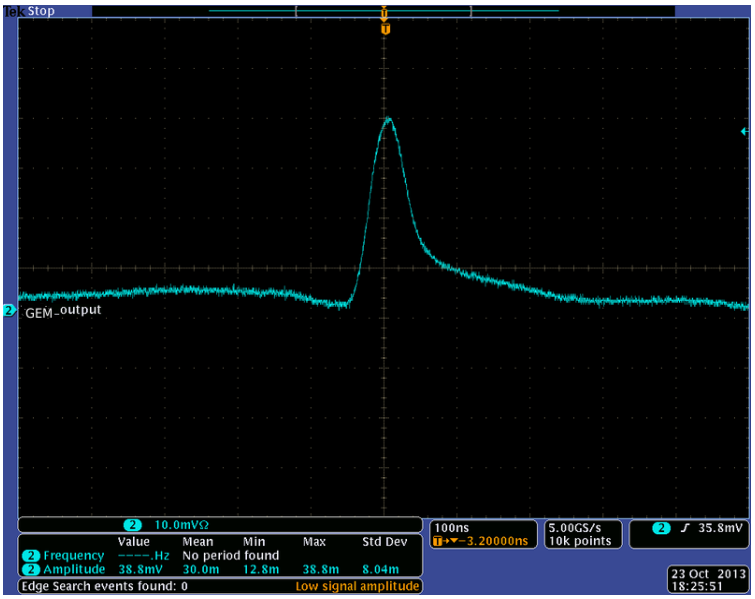

(b)

Figure 4.5: (a) The signal of the fission chamber for open shutter with two peaks(b)and for closed shutter with a longer tail.

4.2.1 Charge Calibration Curve

The QDC was calibrated to measure the equivalent charge for each channel in the QDC spectrum. A known amount of charge was ejected through the same electronic circuit that the QDC used to measure the detector signal and the same integrating gate width of 1 μs. Figure 4.2.1 shows the relationship between the collected charge and the channel number. A linear fit results estimated a slope of 160± 10 fC/ChanNumber. The calibration was used to estimate the charge of each peak in the charge spectrum measured by the QDC as shown in the next section.

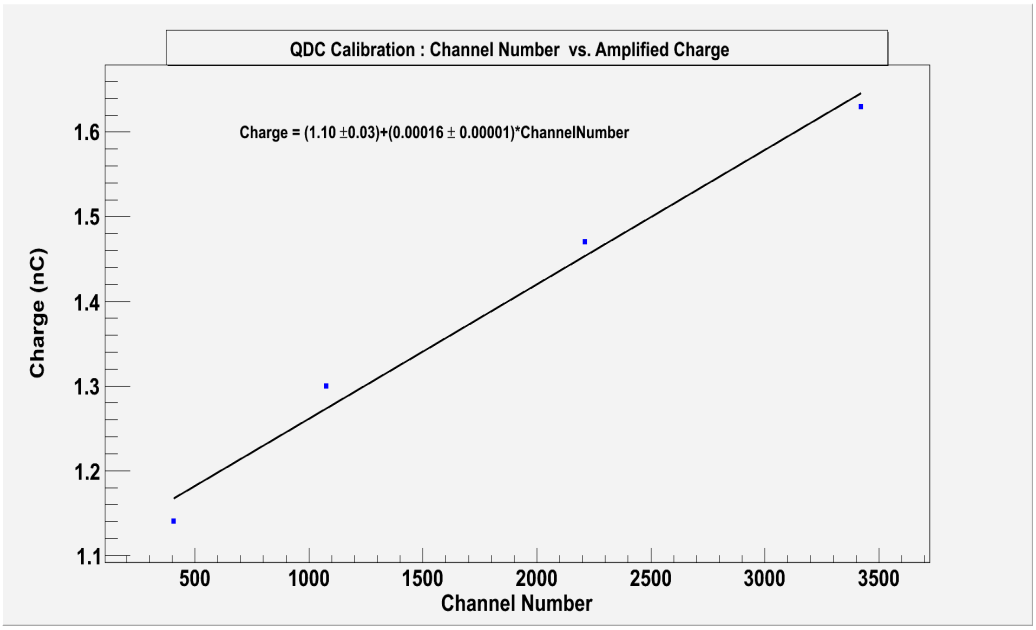

Figure 4.6: Calibration curve of the used QDC with statistical uncertainties smaller than the plotting symbols.

4.2.2 Charge of α-Particles

The QDC measured the charge of ionizing particles when the fiber glass shutter was open and it was closed at two different GEM preamplifier voltages. The measured charge spectra shifted to a higher charge when voltage of the GEM preamplifiers was increased from 2.80 kV to 2.87 kV as shown in Figure 4.7. The shift was expected since the gain increased for the GEM preamplifiers of a higher voltage. Additionally, the rate of each peak dropped after closing the shutter which indicated that the measured charge spectrum represented ionization events that were blocked by the closed fiber glass shutter. At a higher voltage, spectrum showed a higher signal to noise ratio compared to the measured spectrum at lower voltage.

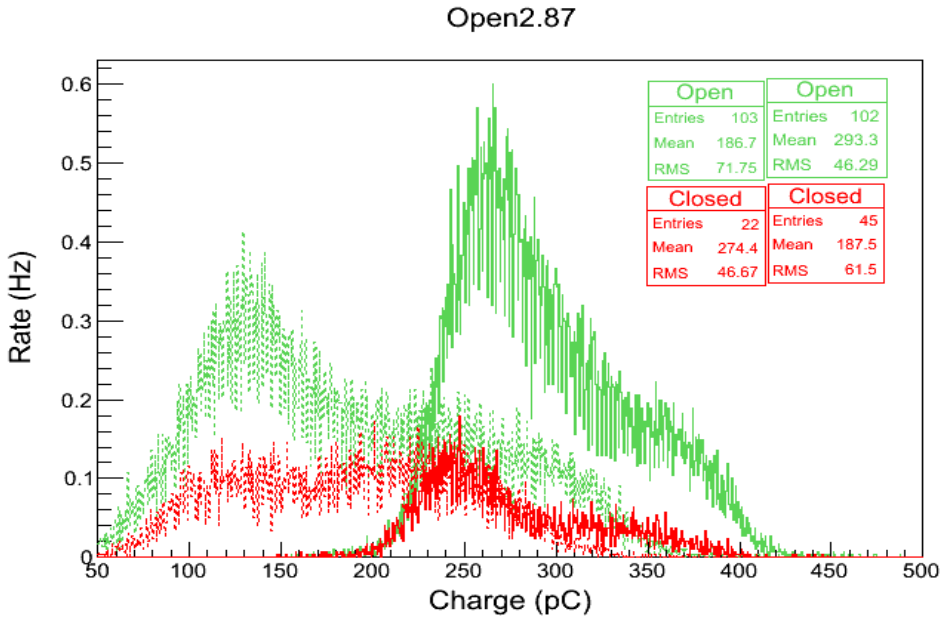

Figure 4.7: The measured charge spectra of open (green) and closed (red) shutter for 2.80 kV (dotted) and 2.87 kV.

Measuring the charge of the ionizing particles emitted from U-233 coating required a two stage approach. The QDC measured the charge for the ionizing particle and its

detection rate when the shutter was open, and when it was closed. Then, the charge spectrum of the closed shutter was subtracted from the charge spectrum measured when the shutter was open as shown in Figure 4.2.2-a. Subtracted spectrum was a measure of the charge liberated by ionizing particles, most likely α-particles that do not penetrate the shutter. According to the simulation results, the charged particles were completely blocked by the closed shutter if they were α-particles of energy less 55 MeV, and the closed shutter measurements would represent a background to the signal of α-particles' ionization.

After closing the shutter, both rates dropped to 0.1 Hz and 0.02 Hz which was 42% and 25% of the rate of particles in open shutter for the first and second peak respectively. Nevertheless, the shutter was unable to stop all the emitted particles due to the unavoidable gap between the U-233 coating and the fiber glass shutter. Therefore, the measured charge for closed shutter was by the emitted particles with an angle in range of 7 degrees to 90 degrees that passed through the gap as shown in Figure 4.8. Those α-particles succeeded to make a signal in the detector because of the shutter diameter which was the same as the U-233 source diameter. The fiber glass shutter shutter could not be larger in diameter due to the limited space inside the chamber.

The second stage was to measure the charged of the ionizing particles accurately after subtracting the pedestal. The QDC measured the pedestal appeared on channel 80 ± 5 (equivalent to 13.1 ± 0.8 pC). The pedestal was measured by the QDC after setting equal voltages on the cathode and the top of the first GEM preamplifier simultaneously during the detector operation. This had the effect of turning the detector off but leaving the GEM preamplifiers on. The pedestal was subtracted to estimate the charge of the ionizing particles collected by the charge collector.

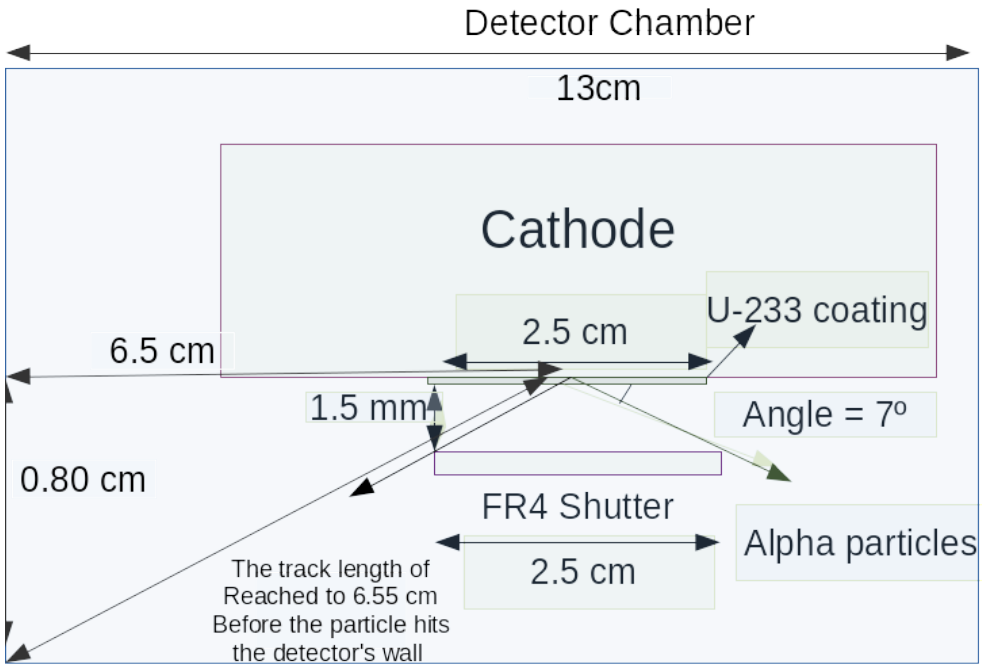

Figure 4.8: The emitted α-particles from the gap between the U-233 coating and the fiber glass shutter.

The average charge for each peak in the QDC spectrum was calculated using the calibration curve and a Gaussian fitting determined the average charge, the standard deviation, and its statistical error. Figure 4.9-b and Figure 4.9-c show a QDC charge spectrum had two peaks when the shutter was open 260±7 pC and 340±31 pC for the first and second peaks respectively after subtracting the pedestal, which was 13±0.8 pC.

The simulation of the ionization of α-particles predicted that an ionization event should liberate 2.4×10^5 and 2.5×10^5 electrons in the drift region for an α-particle of 4.85 MeV and 8.40 MeV respectively. The gas electron multiplier was set to $(8.81\pm0.38)\times10^3$ electrons at 2.87 kV for the GEM preamplifiers and 3.57 kV for the cathode as shown previously in Figure 3.9-b. The collected charge was calculated using the simulation's

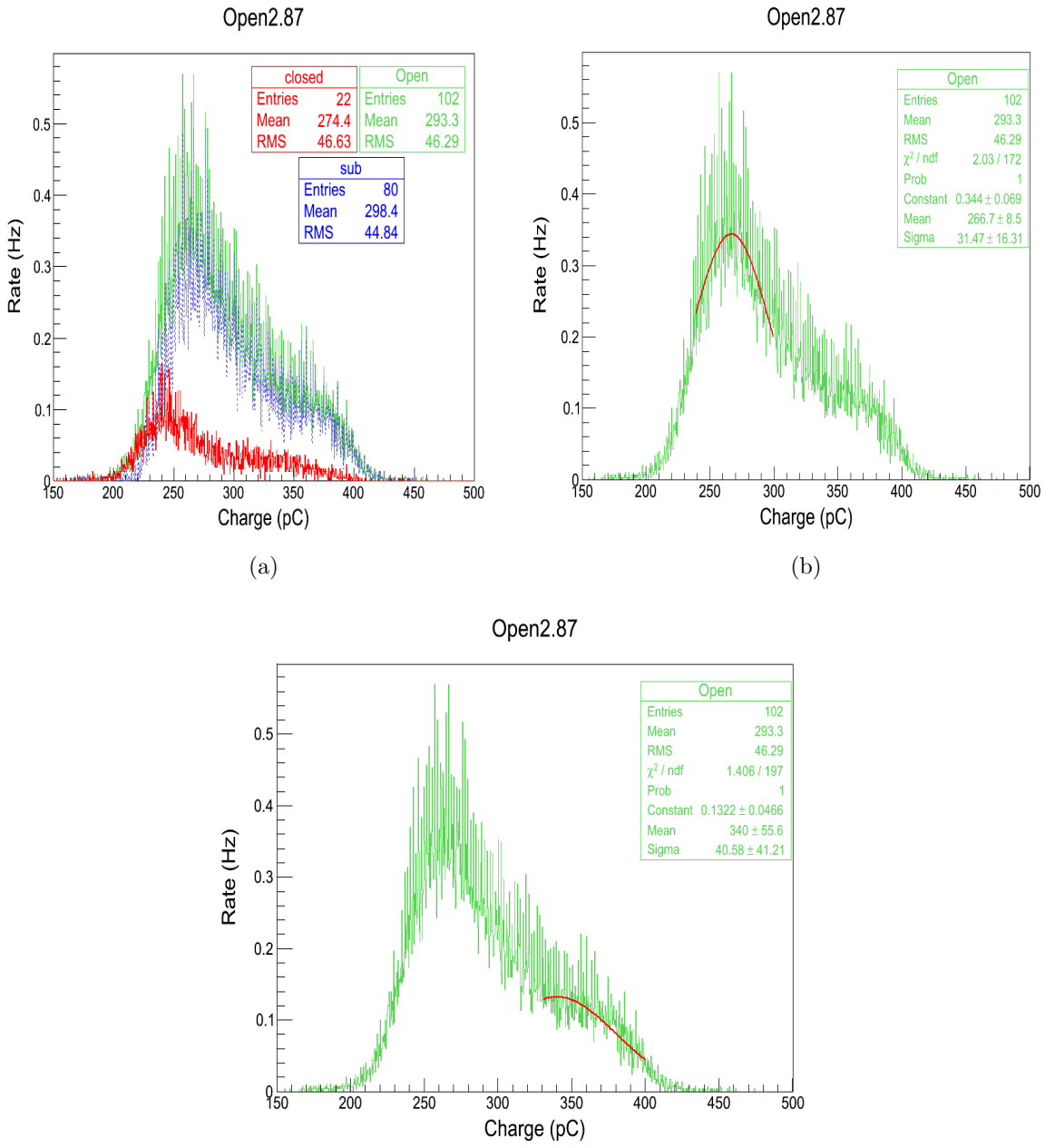

Figure 4.9: Charge spectrum for open and closed shutter for 2.87 kV and 3.87 kV GEM preamplifiers and Cathode voltages respectively (a) Closed spectrum subtracted from open spectrum (subtracted spectrum is the dotted line) (b) Gaussian fitting for the average charge for the first peak and (c)for the second peak.

predictions as shown in Equation 4.3a. The calculated charge was comparable to the average charge

$$\alpha\text{-Particle's Charge} = \text{GEM Gain} \times \text{Ionization Total Charge} \times \text{Electron Charge} \quad (4.1a)$$

$$= 8.807 \times 10^3 \times 2.02 \times 10^5 \times 1.6 \times 10^{-7} pC \quad (4.1b)$$

$$= 284\ pC \quad (4.1c)$$

of the first peak in the QDC charge spectrum with a percentage difference of 9%. Using the same procedure, the predicted charge for 8.4 MeV α-particles (2.5×10^5 secondary electrons) was 352 pC with an percentage difference of 2% as shown in Table 4.2.

α-Energy (MeV)$\pm$0.02	Measured charged (pC)	Predicted charged (pC)	% Difference
4.83	260	284	9%
4.85	260	284	9%
5.80	340	331	3%
6.40	340	352	4%
8.40	340	335	2%

Table 4.2: The measured and the predicted charge for the charge spectrum of U-233 coating for 2.87 kV and 3.87 kV GEM preamplifiers and Cathode voltages respectively.

Additionally, the measured energy spectrum by an α-spectrometer showed a peak of a highest emission rate for 4.85$\pm$0.2 α-particles. The α-spectrometer showed a main peak for α-particles at 4.85$\pm$ 0.02 MeV as shown in Figure 4.2, which gave another evidence of the ionization source for the first peak. Besides the short run spectrum, a long run spectrum was measured for the U-233 coating as shown in Figure 4.10. It showed a lower rate peaks for α-particles of energy higher than 4.85$\pm$0.02 MeV including the ones that had an energy of 8.40$\pm$0.02 MeV. This presented an evidence for the predicted α-energy

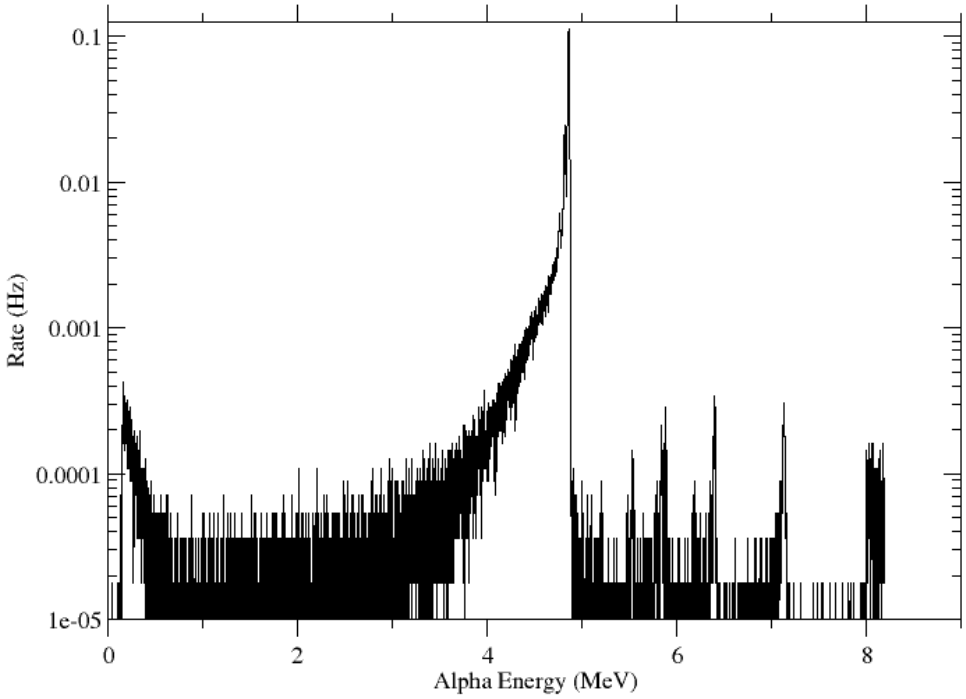

Figure 4.10: Energy spectrum of α-particles emitted from U-233 coating with a run time of 16 hour.

for the second peak. Although the difference percentages were close for 4.85 MeV and 8.4 MeV α-particles, the charge spectrum presented an average charge to include more than one energy for the emitted α-particles as shown in Figure 4.10

4.2.3 Measured Gain of the Triple GEM

The QDC-charge spectrum of α-particles was measured in different voltages to determine the change in the gain of triple GEM detector. The spectrum of α-particles measured when the GEM voltage was in different GEM voltage 2.80 kV and 2.87 kV as shown in Figure 4.11. Calculating the gain was dependent on the first peak in the QDC spectrum when the shutter was open and on the ionization simulation results for the 4.85 MeV α-particles which predicted the number of secondary electrons to be $(2.02 \pm 0.2) \times 10^5$ electrons as previously shown in Figure 3.3.

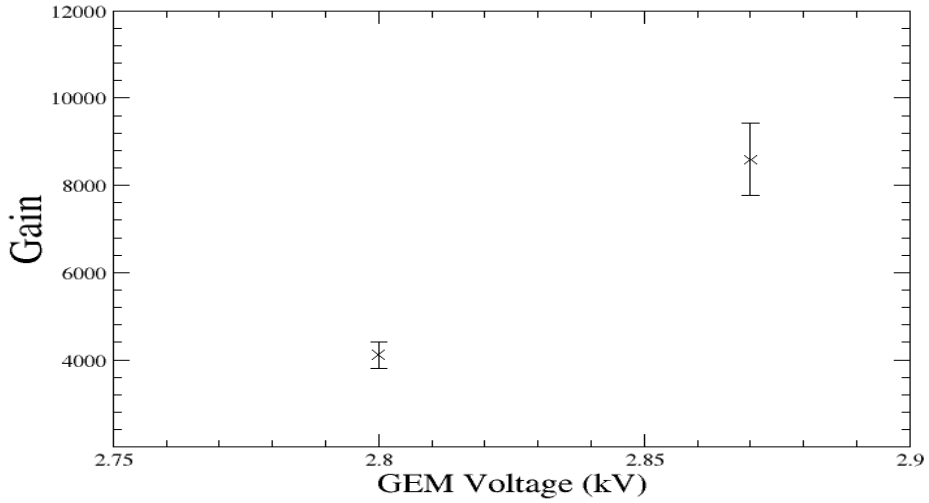

Figure 4.11: The gain measurements using the the first peak of 4.85 MeV α-particle QDC spectrum in 90% Ar-gas and 10% CO_2 gas mixture.

Figure 4.11 shows that the gain increased almost twice when the voltage of the GEM preamplifiers increased from 2.80 kV to 2.87 kV which corresponded to a voltage increment of 7±1 V on each GEM preamplifier. Besides increasing the gain, the standard deviation increased almost twice at 2.87 kV which would decrease the measured charge resolution to from 50% to 35%. Increasing the voltage more than 2.87 kV increased the spark discharge probability caused the protection circuit to trip the power supply.

4.3 Systematic Uncertainties

There were errors and uncertainties in the measured charged liberated by the α-particles. The QDC spectrum of the α-particles was influenced by the voltage on the GEM preamplifiers, and measuring the difference required a high voltage probe with an uncertainty of ± 10. The effect of uncertainty of measuring the voltage decreased when the difference in voltage between the top and bottom of the each preamplifier was calculated, or when the voltage between the cathode and the top of the first GEM preamplifier was estimated to evaluate the drift voltage.

Another factor that contributed in the uncertainty of the measured charge was the fluctuations in the post-amplifier and the other electronic modules. The electronic modules have systematic errors that were dependent on their designs or the environment around them such as the surrounding temperature. The statistical uncertainties of the electronic circuit from the charge calibration was $\pm 1 \times 10^{-5}$ nC/channel in the estimated slope in Figure 4.6 and ± 0.03 nC in the post-amp as shown in Figure 4.12.

The measured charge spectrum using the QDC included both emission rates in an average charge of a standard deviation of ± 31 pC. The first peak represented the average charge of all the emitted α-particles that deposited a charge of 260 ± 31 pC. Similarly, the charge of second peak represented an average charge of α-particles between 5.8 MeV and 6.3 MeV was 340 ± 56 pC as shown in Figure 4.9. Both estimation for the average charge was dependent on the QDC charge calibratiob curve that had a slope of 0.16 ± 0.01 pC. Therefore, the uncertainty in the measured charge by the QDC was estimated as shown in Equation 4.2a.

$$\frac{\Delta(\text{Measured Charge})}{(\text{Measured Charge})} = \frac{\Delta Q_{(\text{calibration})}}{Q_{\text{calibration}}} + \frac{\Delta Q_{\text{Post-amp}}}{Q_{\text{Post-amp}}} \tag{4.2a}$$

$$\Delta(\text{Measured Charge}) = 267(\frac{0.01}{0.16} + \frac{0.03}{1.62}) \tag{4.2b}$$

$$\Delta(\text{Measured Charge}) = \pm 22\ pC \tag{4.2c}$$

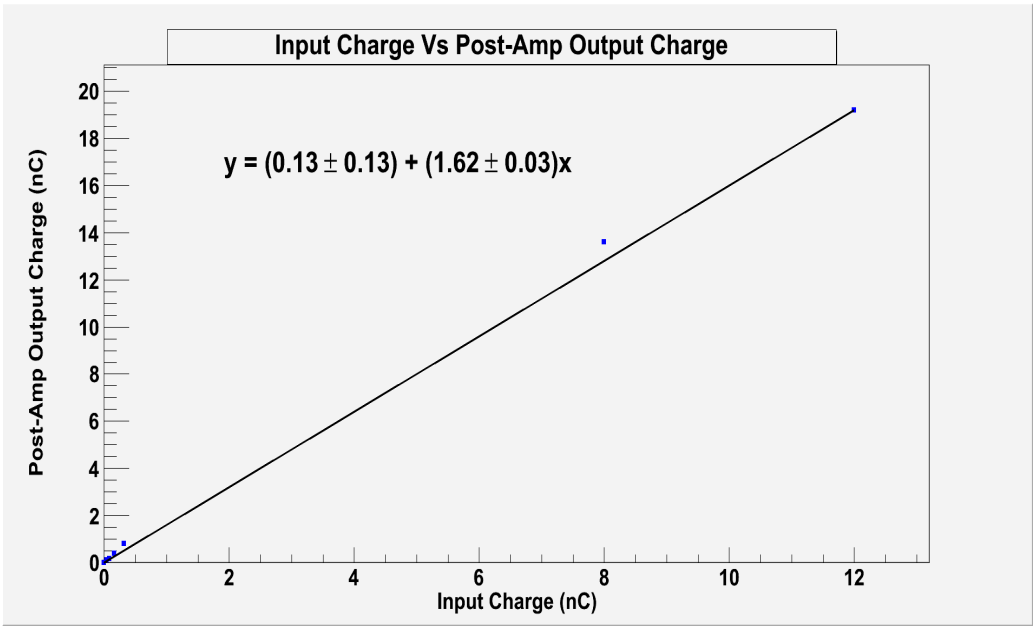

Figure 4.12: linear fitting for the post-amplification output charge before being measured by the QDC.

The uncertainty in the simulated charge using GEANT4 and Garfield for 4.85 MeV α-particles was 12.5 pC considering the uncertainty in the models of ionization cross section in Ar-gas. The uncertainty in the total charge of ionization produced by an α-particle after multiplication was estimated using Equation 4.3a. The total charge of ionization was dependent on the ionization cross section which had 15% uncertainty in the models used in calculating it as shown in Figure 4.13. Therefore, Equation 4.3a was written in terms of the uncertainty of the ionization cross section as shown in Equation 4.3b for an electron flux passing through Ar-gas after an α-particle ionization.

Additionally, GEANT4 used Bethe-Bloch equation that accurately determined the α-particles energy with negligible uncertainty, which was used in determining the number of free electrons produced in Ar/CO_2 gas. The simulation had a default threshold for the ionization of α-particles. Although GEANT4 did not considered the α-ionization defects in the medium, the low threshold did not affect the number of the primary electrons for

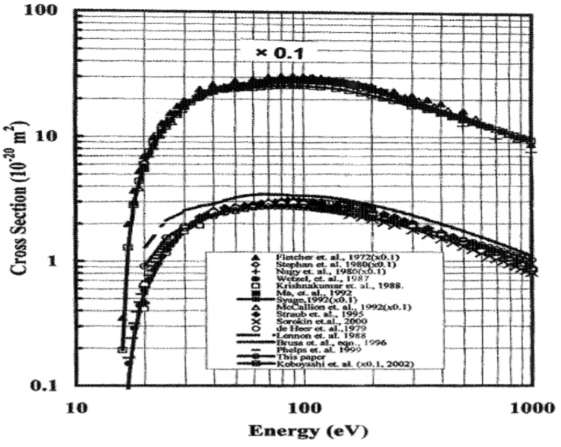

Figure 11. Absolute total ionization cross sections in argon. The data are presented by two curves for more clarity. The values shown by the top curve should be multiplied by 0.1. Experimental: ◆, Fletcher and Cowling, [102]; ◇, Nagy et al., [97]; – –, Wetzel et al., [50]; △, Krishnakumar and Srivastava, [52]; ▲, Ma et al., [97]; ○, McCallion et al., [42], —■—, Syage [41]; □, Straub et al., [103]; ×, Sorokin et al., [86]. Semiempirical values: ● de Heer et al., [55]; — – —, Lennon et al., [90] ——, Brusa et al., [17] ; –, Phelps et al. [100]; ●—●, this paper. Data compiled by the author.

(a)

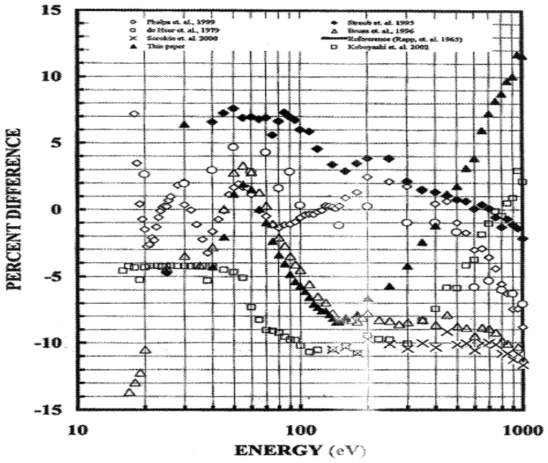

Figure 14. Comparison of total ionization cross sections in argon (continued). Percent difference is calculated with respect to the tabulated values of Rapp and Englander-Golden [84]. ◆, Straub et al. [103]; ×, Sorokin et al. [86]; Semiempirical values and equations: ○, de Heer et al. [55]; △, Brusa et al. [17]; ◇, Phelps and Petrović [100]; ▲, this paper, equation (24). Data calculated according to equation (23) are not shown as they fall outside the band of ± 15%.

(b)

Figure 4.13: Argon gas ionization measurements and models

the α-particles since they left the drift region with an energy higher than the ionization defect energy. As a result, the uncertainty in the models of electron ionization cross in Ar-gas was the main source of the certainty in the simulated charge after the electron multiplication as shown in Equation 4.3b.

$$\frac{\Delta(\text{Simulated Charge})}{(\text{Simulated Charge})} = \frac{\Delta(\text{GEM Gain})}{(\text{GEM Gain})} + \frac{\Delta Q_{\alpha\text{-Ionization}}}{Q_{\alpha\text{-Ionization}}} \tag{4.3a}$$

$$\frac{\Delta(\text{Simulated Charge})}{(\text{Simulated Charge})} = \frac{\Delta\sigma_e}{\sigma_e} \tag{4.3b}$$

$$\Delta(\text{Simulated Charge}) = 284(\frac{0.15 \times 10^{-20}}{1 \times 10^{-20}}) \tag{4.3c}$$

$$\Delta(\text{Simulated Charge}) = \pm 43\ pC \tag{4.3d}$$

Chapter 5

Conclusion

A fission chamber equipped with gas electron preamplifiers was designed, constructed, and tested. A cathode containing a thin film of U-233 was installed to make the ionization chamber sensitive to neutrons and to provide a source of α-particles that would ionize the gas inside the chamber. A set of three gas electron multipliers were stacked on top of each other to preamplifier the ionization signal. A summary of the detector's performance is given below.

Increasing the size of the drift region increased the deposited charge in it. The height of the drift region increased to become 1 cm which increased the measured number of free electrons for a 4.85 MeV α-particles to reach $(2.02 \pm 0.20) \times 10^5$ electron. However, the difference in the deposited charge of the incident α-particles should be at least 27$\pm$ 11 pC when the fission chamber was operated at 2.87 kV and 3.57 kV for the GEM preamplifiers and the cathode respectively and had 35% charge resolution.

GEANT4 simulated the number of free electrons in the drift region for β and γ-particles when the scattering process was included along with the ionization. The number of free electrons was 100 electrons for β-particles of energy of exceeded 100 keV as predicted by GEANT4 and ESTAR software packages. In addition, each emitted photon from the U-233 coating liberated a single free electron since their energies are within the photo-absorption limits. Therefore, the predicted contribution of β and γ-particles were negligible for a 100 keV β-particles and all the photons that might liberate photo-electrons within the same energy range. The prediction was dependent on the U-233 coating emission rate which was considered very low compared to the emitted α-particles or to photon rates mixed with any neutron flux.

GEANT4 simulations were performed to calculate the charge of each emitted particle from the U-233 coating in the drift region. In a 90% Ar-gas and 10% CO_2 gas mixture, ionization was the main interaction in GEANT4 simulation that was used in calculating the number of primary and secondary electrons in drift region. The α-particles produced $(2.02 \pm 0.20) \times 10^5$ free electrons when their incident energy 4.85 MeV. It is largest number of secondary electrons produced in the drift region (2×10^3 folds) compared to the other emitted particles in the drift region.

The measured charge spectrum by the QDC had two peaks, the first peak matched the simulated deposited charge of 4.85 MeV α-particles. The Garfield and GEANT4 simulation for the deposited charge of the 4.85 MeV α-particles in the drift region agreed with the first peak of a charge of 260 pC and a percentage difference of 9%. GEANT4 predicted 2.02×10^5 liberated electrons by ionization in the drift region. Garfield predicted the multiplication of the triple GEM preamplifiers which was $(8.81 \pm 2.5) \times 10^3$ electrons at 2.87 kV and 3.57 kV for the GEM preamplifiers and the cathode respectively.

The charge of the second peak matched GEANT4 and Garfield simulation for α-particles of energy of 6.40 MeV. The predicted number of free electrons liberated by the 8.40 MeV was $(2.38 \pm 0.20) \times 10^5$ electrons which made the predicted charge collected by the charge collector reached 335 pC after electron multiplication to have a percentage difference of 2%.

Although the measured and the predicted charge for the first and the second peak were very close with less than 9% percentage difference, the standard deviation reach 31 pC for each peak. The measured charge charged spectrum had a low charge resolution, the average charge of the first peak was 260$\pm$31 pC for both energies 4.85$\pm$0.02 MeV and 4.83 $\pm$0.02 MeV and the average charge of the second peak was 340 pC for 5.8 MeV to 8.4 MeV α-particles.

The predicted average charge carried by the signal of the light and heavy fission fragments after the GEM multiplication of $(8.81 \pm 2.5) \times 10^3$ electrons are 1.53×10^{12} for 7.13×10^{11} electrons. Each fission fragment liberated 1.7×10^6 and 0.8×10^6 secondary

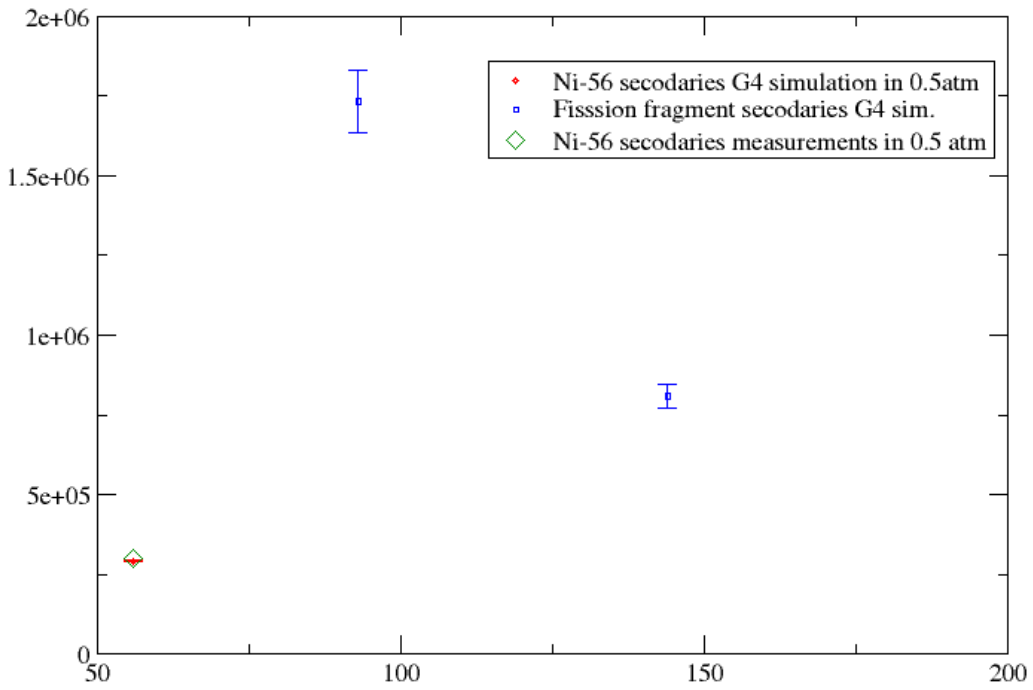

Figure 5.1: Simulation of the secodary electrons of heavy and light fission fragments from a fission event of a induced neutron and U-233 atom.

electrons for light and heavy fission fragments respectively as shown in Figure 5.1. Although the fission chamber distinguish the type of the fission fragments, the gain of the fission chamber should be decreased to avoid any probability of spark discharge in the fission chamber.

The advantage of a lower gain is to use the fission chamber in the pulse mode during the neutron fluence test. Increasing the energy limit of low ionizing particles (photons and electrons) to contribute in the detector signal is expected when the gain of

the fission chamber decreases. Therefore, the detector detection rate to photons decreases for photons which helps to use the detector in the pulse mode with an expected detection rate of 5 MHz.

The statistical uncertainties were estimated for the gain of the GEM preamplifiers simulated by Garfield and the number of secondary electrons simulated by GEANT4. The statistical error in the mean and standard deviation for the estimated gain by simulation was ±383 electrons and ±544 electrons respectively. However, the benchmarked data for gain of 93% Ar-gas and 7% CO_2 gas mixture showed a 25% increment when the difference in voltage was 340 V on GEM preamplifier. Therefore, the simulated gain by Garfield expected an increment of 25% at the maximum limit which agreed with the estimated standard deviation of 2.5×10^5 electrons. Similarly, GEANT4 had a standard deviation for the secondary electrons of 2×10^3 electrons which agreed with the benchmarked data simulation.

The uncertaity in the measured and the simulated charge were calculated using the least square method. The uncertainty in the measured charge was ±22 pC using the unceraity in the slope of the QDC calibration curve and the uncertanity in the post-amp amplifcation. Additionally, the uncertainty in simulated charge using GEANT4 and Garfield was ±43, which appeared because of the variety in the electron ionization models that estimated the electron ionization cross section within an error of ±15%.

Bibliography

[1] K. Hyde, Perlman I., and G.T. Seaborg. *The Nuclear Properties of the Heavy Elements: Fission phenomena*. The Nuclear Properties of the Heavy Elements. Dover Publications, 1971.

[2] LANL. Index to endf/b-vii.1 decay data. `https://t2.lanl.gov/nis/data/endf/decayVII.1.html`.

[3] J. Rasmussen. Alpha-decay barrier penetrabilities with an exponential nuclear potential: Even-even nuclei. *Phys. Rev.*, 113:1593, 1959.

[4] Michael F. L'Annunziata. *Handbook of Radioactivity Analysis*. Academic Press, 2003.

[5] NIST. Xcom. `http://physics.nist.gov/PhysRefData/Xcom/html/xcom1.html`.

[6] N.J Carron. *An Introduction to the Passage of Energetic Particles through Matter*. CRC Press, 2006.

[7] S. Agostinelli. Geant4a simulation toolkit. *NIM A*, 506(3), 2003.

[8] J. Ziegler. Srim - the stopping and range of ions in matter. *NIM B*, 268(11-12), 2010.

[9] Edward A. Mason and Earl W. McDaniel. *Transport Properties of Ions in Gases*. Wiley-VCH, 1988.

[10] Yuri P. Raizer. *Gas Discharge Physics*. Berlin:pringer, 1991.

[11] M. Facina. A gas catcher for the selective production of radioactive beams through laser ionisation. Master's thesis.

[12] John Kuffel and Peter Kuffel. *High Voltage Engineering Fundamentals, Second Edition*. Newnes, 2000.

[13] F. Sauli. Principles of operation of multiwire proportional and drift chambers. `http://cds.cern.ch/record/117989`, 1977.

[14] L.G.H. Huxley and R. W. Crompton. *Diffusion and Drift of Electrons in Gases (Wiley series in plasma physics)*. John Wiley & Sons, 1974.

[15] S. Biagi. Magboltz. `Http://magboltz.web.cern.ch/magboltz/`.

[16] CERN. Garfield. `http://garfieldpp.web.cern.ch/garfieldpp`.

[17] F. Sauli A.Sharma. First townsend coefficient measured in argon based mixtures at high fields. *NIM A*, 334(420-424), 1993.

[18] S. et al Chabod. Modelling of fission chambers in current modeanalytical approach. *NIM A*, 566(2), 2006.

[19] Technische University Munchen Physik Department E18. 2d readout plane. `http://www.e18.ph.tum.de/research/compass/gempixelgem-tracking-detector%s`.

[20] L. et al Shekhtman. Gem-based detectors for sr imaging and particle tracking. *Inst. Journal of Instrumentation*, 7(3), 2012.

[21] J. Franck. Gem tracking detectors for compass. `https://www.e18.ph.tum.de/research/compass/gempixelgem-tracking-detecto%rs/`.

[22] R. Dunker. *quantitaties data*. Environmental lab-ISU, August 2015.

[23] F. Sauli et al. Gem: A new concept for electron amplification in gas detectors. *NIM A*, 386(2-3):531–543, 1997.

[24] C.Shalem R.Chechik, A.Breskin. Thick gem-like hole multipliers: properties and possible applications. *NIM A*, 535(1-2):303–308, 2004.

[25] CERN European Organization for Nuclear Research Physics Departmen. Rd51. `http://rd51-public.web.cern.ch/RD51-Public/`.

[26] S. Pinto. Gas electron multipliers development of large area gems and spherical gems. Master's thesis, Mathematisch-Naturwissenschaftliche Fakultt, 2011.

[27] CAEN S.P.A. V792. `http://www.caen.it/csite/CaenProd.jsp?idmod=41parent=11`.

[28] IAEA. *INDC(BLR)-016*. IAEA, 2003.

[29] Fabio Sauli. *Basic processes in gaseous counters. In Gaseous Radiation Detectors: Fundamentals and Applications*. Cambridge University Press, 2014.

[30] K. et al Saito. Simultaneous measurements of absolute numbers of electrons and scintillation photons produced by 5.49 mev alpha particles in rare gases. *IEEE TRANSACTIONS ON NUCLEAR SCIENCE*, 50(6), 2003.

[31] C.C. Hanke and H. Bichsel. *Precision Energy Loss Measurements for Natural Alpha Particles in Argon*. Danske Videnskabernes Selskab. Matematisk-fysiske Meddelelser v. 38. Department of Physics, University of Southern California, 1970.

[32] M. et al Jurado. Dependence of self-absorption on thickness for thin and thick alpha-particle sources of uo2. *NIM A*, 548, 2005.

[33] WNA. Uranium and depleted uranium. `http://www.world-nuclear.org/info/Nuclear-Fuel-Cycle/Uranium-Resources/%Uranium-and-Depleted-Uranium/`, 2014.

[34] NIST. Estar. `http://physics.nist.gov/PhysRefData/Star/Text/ESTAR.html`.

[35] Geant4 physics manual. `http://geant4.web.cern.ch/geant4/UserDocumentation/UsersGuides/PhysicsR%eferenceManual`, 2010.

[36] CERN. Documentation. `http://garfieldpp.web.cern.ch/garfieldpp/documentation`.

[37] CERN. Heed. `http://ismirnov.web.cern.ch/ismirnov/heed`.

[38] ANSYS Academic Research. Ansys release 15.0. `ANSYS.com`.

[39] D. Zuydtwyck. Development of micro-pattern gaseous detectorsgem. Master's thesis, Ludwig-Maximilians-Universitat in Munchen.

[40] M. et al ungwirth. Determination of the photon spectrum in an intense fission neutron beam. *Journal of Instrumentation*, 3(22), 2012.

[41] CERN. Root : A data analysis framework. `https://root.cern.ch/drupal`.

[42] Canberra. Canberra 7401. `http://www.canberra.com/products/radiochemistrylab/alpha-spectroscopy.a%sp`.

[43] ORTEC. Ortec 926. `http://www.ortec-online.com/download/926-MNL.pdf`.

Appendix A

Solving Boltzmann Equation

A.1 Solving Boltzamn Equation for a Hole of Uniform Electric Field [14]

Asymptotic solution details for Boltzmann Equation A.1 for a hole has a uniform electric field takes the form in Equation A.2.

$$D(\frac{\partial^2}{\partial x^2} + \frac{\partial^2}{\partial x^2})n + D_L\frac{\partial^2}{\partial z^2} - W\frac{\partial}{\partial z}n = 0 \tag{A.1}$$

$$n(x', y', z') = e^{\lambda_L z'}V(x, y, z) \tag{A.2}$$

$$\nabla'^2 V = \lambda_L^2 V \tag{A.3}$$

$$\nabla'^2 V = \frac{\partial^2}{\partial x'^2} + \frac{\partial^2}{\partial y'^2} + \frac{\partial^2}{\partial z^2} \tag{A.4}$$

$$x' = \frac{D_L}{D}xy' = \frac{D_L}{D}y \tag{A.5}$$

Using spherical coordinates, Equation A.3 as be written as in Equation A.6 which is symmetric in ϕ direction.

$$\frac{1}{r'^2}\frac{\partial}{\partial r'}r'^2\frac{\partial V}{\partial r'} + \frac{1}{r'^2 sin\theta'}\frac{\partial}{\partial \theta}sin\theta\frac{\partial V}{\partial \theta} = \lambda_L^2 V \tag{A.6}$$

Assuming $V(r', \theta) = R_k(r')P_k(\mu)$ the solution of the zenith angle direction is the Legendre polynomial, and can be written as shown in the Equation A.7.

$$\frac{1}{r' sin\theta}\frac{\partial}{\partial\theta}sin\theta\frac{\partial V}{\partial\theta} = R_k(r')\frac{d}{d\mu}\left[(1-\mu^2)\frac{dP_k(\mu)}{d\mu}\right] \tag{A.7}$$

and

$$\frac{d}{d\mu}\left[(1-\mu^2)\frac{dP_k(\mu)}{d\mu}\right] = -k(k+1)P_k(\mu) \tag{A.8}$$

so,

$$\frac{1}{r'^2}\frac{d}{dr'}\left(r'^2\frac{dR_k}{dr'}\right) - \left[\frac{k(k+1)}{r'^2} + \lambda_L^2\right]R_k = \frac{d^2R_k}{dr'^2} + \frac{2}{r'}\frac{dR_k}{dr'} - \left[\frac{k(k+1)}{r'^2} + \lambda_L^2\right]R_k = 0 \tag{A.9}$$

The modified Bessel functions, first and second kind, are the solutions for the previous equation but the boundary conditions determines which one to use, in this case $r' \rightarrow 0$, n $\rightarrow \infty$, and n $\rightarrow 0$ as $r' \rightarrow \infty$. so only the modified Bessel of second kind K_k are the non-zaro terms. so the general solution for the equation is shown in A.10.

$$V = R_k(r')P_k(\mu) = \exp(\lambda_L z)\sum_{k=0}^{\infty} A_k r'^{-1/2}K_{k+1/2}(\lambda_L r')P_k(\mu) \tag{A.10}$$

The general form of the previous equation and its solution are defined as shown in the Equations A.11, A.12.

$$\frac{d^2y}{dx} + \frac{1-2\alpha}{x}\frac{dy}{dx} - \left[\frac{\nu^2\gamma^2 - \alpha^2}{x^2} + (\beta\gamma x^{\gamma-1})^2\right]y = 0 \tag{A.11}$$

$$y = x\alpha I_\nu(\beta x^\gamma) \tag{A.12}$$

$$y = x\alpha K_\nu(\beta x^\gamma) \tag{A.13}$$

where I_ν and K_ν are the modified Bessel of the first and the second kind.

In case of of solving for the density number outside the hole, then the solution contains only the modified Bessel of the second kind K_ν, also applying the boundary

conditions below n = 0, when z = 0, and as $r > a$ where a is the hole radius. It implies that $P_k = 0$ if k is odd, so the solution can be written as shown below.

$$n = R_k(r')P_k(\mu) = \exp(\lambda_L z)\sum_{k=0}^{\infty} A_k r'^{-1/2} K_{k+1/2}(\lambda_L r')P_k(\mu) \tag{A.14}$$

In case of GEM preamplifer $r >> a$, since each hole has a radius of 50 um, and the electron streams appear in a millimeter scale distance. So A_ks' values decrease since it is a function of λ_La ($\lambda_L a << 1$), so the higher order terms become negligible compared to the first (monopole) and the second (dipole) term. Then the solution can be written for the dipole term (anisotropic diffusion) :

$$n = A_1 \exp(\lambda_L z) r'^{1/2} K_{3/2}(\lambda_L r')P_1(\mu) \tag{A.15}$$

and for the monopole term,(isotropic diffusion).

$$n = A_0 \exp(\lambda_L z) r'^{1/2} K_{1/2}(\lambda_L r')P_0(\mu) \tag{A.16}$$

where:

$$K_{1/2} = (\frac{\pi}{2\lambda_L r'})^{1/2} e^{-\lambda_L r'} \tag{A.17}$$

$$K_{3/2} = (\frac{\pi}{2\lambda_L r'})^{1/2}(1 + \frac{1}{\lambda_L r'})e^{-\lambda_L r'} \tag{A.18}$$

So :

$$n_{monopole} = (\frac{\pi}{2\lambda_L})^{1/2}\frac{e^{-\lambda_L(r'-z)}}{r'} \tag{A.19}$$

$$n_{dipole} = (\frac{\pi}{2\lambda_L})^{1/2}\frac{z}{r'}(1 + \frac{1}{\lambda_L r'})\frac{e^{-\lambda_L(r'-z)}}{r'} \tag{A.20}$$

$$-\frac{\partial}{\partial r'}n_{monopole} = -(\frac{\pi}{2\lambda_L})^{1/2}\frac{\partial}{\partial r'}\frac{e^{-\lambda_L(r'-z)}}{r'} \tag{A.21}$$

for $r' = \sqrt{\rho'^2 + z^2}$